

Estimating the Far-Field Radiation Pattern from Near-Field Measurements using an Automated Robotic Arm

Near-Field to Far-Field Transformation Program for Customizable
Scanning Geometry.

Matthieu Gillain
Danylo Zavoloko

in partial fulfilment of the requirements for the degree of

Bachelor of Science
in Electrical Engineering

Students & Authors	Matthieu Gillain Danylo Zavoloko	5610052 5557275
Supervisors	Prof. Dr. Nuria Llombart Msc Dunja Lončarević	
Jury chair	Dr. Marco Spirito	
Jury member 1	Dr. Daniele Cavallo	
Jury member 2	Dr. Ir. Moritz Fieback	



Abstract

Automated Robotic arms redefine the limits of antenna characterization. This paper presents a method to estimate the far-field radiation pattern of antennas utilizing near-field measurements through the use of a 6-axis robotic arm. The innovation of our project lies in overcoming the current limitation of fixed scanning geometries, by extending them to any possible spatial shape with the support of a 6-axis robotic arm.

The project is built and validated incrementally through a series of MATLAB functions, utilizing the equivalence theorem as a NF to FF transformation method. Each stage builds upon the previous ones and increases in complexity. Validation stages begin by simulating infinitesimal dipoles and progress up to experimental validation of a tilted horn antenna. All the validation steps are successfully met, except for an unexpected phase symmetry.

Our work sets a solid foundation for further development of this antenna measurement system. The system will significantly improve antenna characterization by enabling more flexible scanning grids.

Contents

1	Introduction	2
1.1	Today's Challenge	2
1.2	Objective of the Project	2
1.3	State-of-the-art Analysis	3
1.3.1	Usage of Robotic Arm	3
1.3.2	NF to FF Transformation	4
1.4	Requirements of the Project	5
1.4.1	Requirements of the Complete Project	5
1.4.2	Requirements of the NF-to-FF Program	5
1.5	Context of the Project & Distribution of Tasks	6
1.6	Outline of Thesis	6
2	Basic Antenna Theory	8
3	Methodology	12
3.1	Definition of Reference System & Grids	12
3.2	Validation steps	16
3.2.1	Single Dipole at the Origin	17
3.2.2	Single Dipole Shifted by 5 cm	18
3.2.3	Dipole Grid	18
3.2.4	Normal Oriented Horn Antenna at Origin	19
3.2.5	Tilted Horn Antenna at Origin	19
3.2.6	Experimental Validation	19
3.3	Obtaining the Directivity	22
3.4	Plotting Results	22
3.4.1	UV Plots	22
3.4.2	Cuts of the Magnitude	22
4	Program Structure & Functionality	23
4.1	Setting Up & Viewing the Grids	23
4.1.1	Implementing the Near-Field Grid	23
4.1.2	Implementing the far-field grid	24
4.2	Storing and Transferring the Measured Data	24
4.3	Simulating & superimposing the dipole E-fields	25
4.4	Directivity	26
4.5	Plotting	26
5	CST Simulation	27
5.1	Environment Setup	27
5.2	Dipole Simulations	28
5.3	Export Setting and Post-processing	28
5.4	Other Dipole Configurations	28
5.5	Horn Simulation	28
5.6	Rotated Horn Antenna at Origin	29

6 Results & validation	30
6.1 Single Dipole at the origin	30
6.2 Single dipole along X, shifted by 5 cm	30
6.3 Dipole Grid	31
6.4 Horn antenna at the origin	31
6.5 Tilted horn antenna at the origin	31
6.6 Experimental Validation	31
6.6.1 Normal Oriented Horn antenna at the origin	31
6.6.2 Tilted horn antenna at the origin	33
6.6.3 Directivity	33
7 Summary, Discussion & future work	35
7.1 Summary	35
7.2 Discussion & Future Work	35
A Appendix	40
B MATLAB results	41
B.1 Single dipole at origin along X	41
B.2 Single dipole at origin along Y	44
B.3 Single dipole at origin along Z	46
B.4 Single Dipole along X, shifted by 5 cm	48
B.5 Grid of 3x3 dipoles along X spaced by $\lambda/2$, centred at the origin.	51
B.6 Horn Antenna at the Origin	53
B.7 Tilted Horn Antenna at Origin	58
B.8 Experimental Horn Antenna at the Origin	61
B.9 Experimental Tilted Horn Antenna at the Origin	63
C CST simulations	64
C.1 CST export setting	64
C.2 CST data, plot by MATLAB	66
C.3 Near-field export settings	70
C.4 Rotated Far-Field	71

1 Introduction

Antennas are at the core of many modern wireless communication and sensing systems, ranging from satellite communications to medical imaging. The quality of the transmitted and received signals is a direct consequence of the performance of the antenna used in the wireless system. However, practical radiation can differ from antenna theory. Thus, accurate antenna measurements are needed to provide realistic insights into the antenna's performance and *usability in real-world applications*. Antenna measurement also precedes any product development or an experiment involving an antenna.

1.1 Today's Challenge

Radiation pattern measurement is typically done in large anechoic chambers [1]. The radiation pattern of the antenna under test (AUT) is measured with a reference antenna in the far-field or with a probe (open waveguide) in the near-field. To do so, a vector network analyser (VNA) transmits a signal through the AUT and measures the signal received by the reference antenna. To accurately characterize the antenna's full radiation pattern, measurements must be taken at multiple points around the antenna, as the radiated field varies with direction [2]. Note that the ensemble of points where a measurement is taken is called the measurement grid or scanning grid. Rotational and linear actuators can be used to move one of the antennas in order to measure the radiation at different locations, and thus form the scanning grid. However, this scanning grid is fixed as the actuators provide limited degrees of freedom. Hence, different antennas with different wavefronts may not be accurately measured, if the shape of the wavefront does not match the shape of the measurement grid. For example, horn antennas have a spherical wavefront while lens antennas have a planar wavefront: measuring a horn antenna with a planar grid is ineffective, as is measuring a lens antenna with a spherical grid. Figure 1 illustrates this challenge. In traditional measurement set-ups, researchers are often limited to planar or spherical measurement grids, in the near-field or far-field of the AUT [3][4]. Figure 27 shows such an anechoic chamber. In that particular set-up, researchers are limited to spherical scanning grids as the AUT can rotate on the turntable (rotational actuator).

1.2 Objective of the Project

The innovation of our project lies in overcoming the limitation to fixed scanning geometries by extending them to any possible spatial shape with the support of a 6-axis robotic arm. This is useful for measuring the antennas with different wavefronts. For example, horn antennas have a spherical wavefront and lens antennas have a planar wavefront, Figure 1. Also, the user may require a spherical grid for antennas with a broad beam, or a planar grid for highly directive antennas [1], [5].

A probe, connected to the vector network analyser (VNA), is placed at the extremity of a 6-axis robotic arm, as depicted by Figure 2. It can therefore reach nearly every position in a given 3D volume, and is only limited by the maximum reach of the arm and by physical objects in the set-up (e.g. the table on which the antenna is placed).

The far-field radiation (FF) is one of the most important figures of merit of any antenna. However, the far field radiation may be impossible to measure directly, as it can be at large distances

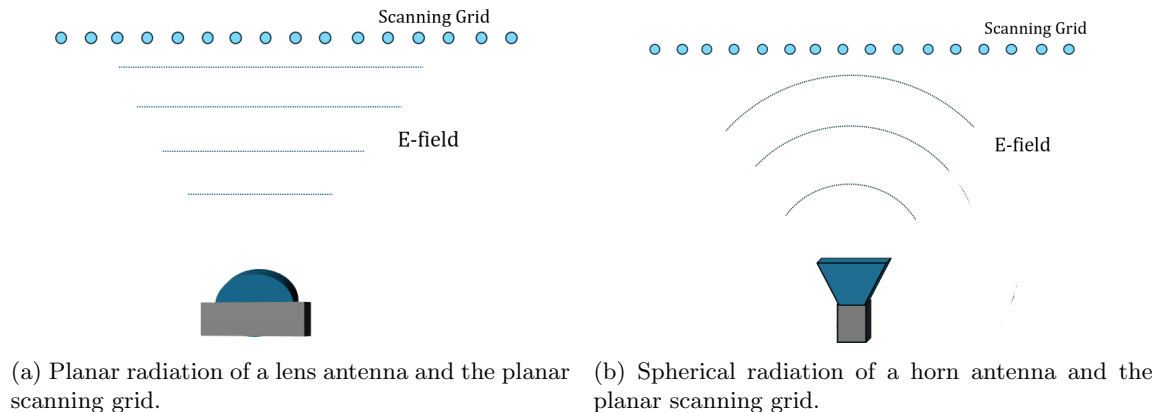


Figure 1: Two types of antennas with different radiation but identical scanning grid.

from the AUT. This can be the case due to frequency or aperture size. Such distances often exceed the robotic arm's reach. Therefore, for those cases, it is easier to measure the near-field (NF) and transform it to FF radiation pattern. This work aims to develop a MATLAB program that uses near-field measurements to estimate the far-field radiation pattern, bridging the gap between practical measurement limitations and accurate far-field characterization. The NF-to-FF transformation is done using the intuitive equivalence theorem[6], [7]. A schematic overview of the set-up is depicted in Figure 2. Please note that the aim of the project is to introduce the robotic arm measurement set-up in the THz sensing group, TU Delft, host of this project. Using robotic arms to measure antennas is not new.

1.3 State-of-the-art Analysis

This section analyses recent research and developments on the use of a robotic arm to measure the near-field in order to estimate the far-field.

1.3.1 Usage of Robotic Arm

The use of robotic arms to take antenna measurements has been in development for years. Robotic arms offer an increased flexibility in terms of scan geometry compared to traditional methods, that offers adaptability to different antenna types [3], [8], [9]. A primary challenge in the development of such measurement systems has been the positioning errors of the robotic arm [3], [10]. At higher frequencies, as the wavelength becomes smaller, these positioning errors can provoke inaccurate measurement of the radiation [8]. Error reduction techniques have been explored; [8] uses coordinated spatial metrology and [11] provides a numerical method to estimate the error and uncertainty in the measurements. Furthermore, research has been conducted to reduce the scanning time or scanning volume. [12] reduced the scanning volume by 49.9% and motion time by 17.7% by introducing a dual robotic arm system. [13] reduces the scanning time by implementing a novel algorithm that reduces the amount of sampling points. [14] offers a study on the practical implications of a compact robot setup for Over-the-Air Measurements.

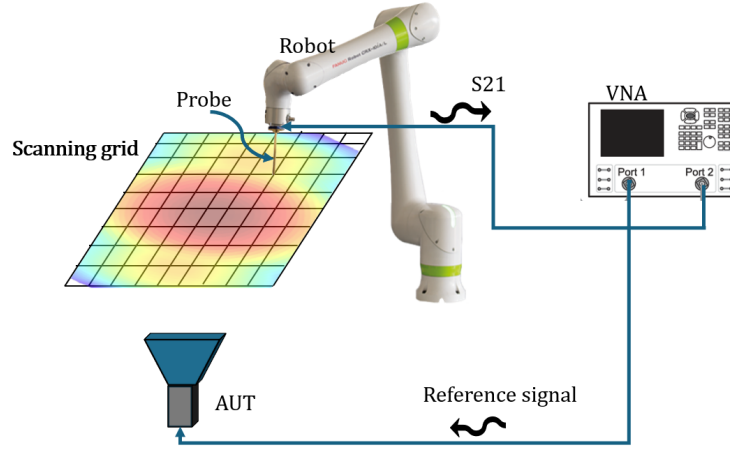


Figure 2: Overview of measurement set-up.

1.3.2 NF to FF Transformation

The challenge of directly measuring the far-field is well known. Techniques to estimate the far-field radiation based on near-field measurements are therefore well researched.

[15] equalizes differences in the results of multiple transformation techniques. Specifically, spherical, cylindrical and planar algorithms are studied for use with a multi-axis robot, irrespective of scanning geometry or probe. [4] explains that current NF-to-FF transformation methods (e.g. Fast Fourier Transform) are very efficient and robust. Importantly, future NF-to-FF methods will need to perform well with the introduction of the robotic arm.

1.4 Requirements of the Project

1.4.1 Requirements of the Complete Project

- (1) Must: Control a 6-axis robotic arm for executing both planar and spherical measurement patterns.
- (2) Must: Perform measurements in both near-field (NF) and far-field configuration.
- (3) Must: Give the user flexibility in terms of system parameters.
- (4) Must: Support near-field to far-field transformation to estimate far-field radiation pattern from NF data.
- (5) Must: Plot the results obtained from the NF-to-FF transformation.
- (6) Must: Provide a user interface (UI) for controlling the robotic arm, starting measurements and visualising results.
- (7) Must: Operate autonomously with minimal user intervention once measurements are configured.
- (8) Must: Be generic. Support any scanning geometry.
- (9) Must: Be well organized for further development.

1.4.2 Requirements of the NF-to-FF Program

- (1) Must: Use the equivalence theorem as NF-to-FF transformation method.
- (2) Must: Be able to execute the transformation using data points from CST.
- (3) Must: Take into account antenna theory.
- (4) Must: Deliver a planar scanning grid in the XY-plane.
- (5) Must: Deliver a tilted planar scan configuration.
- (6) Must: Plot the raw measurement data.
- (7) Must: Plot the results obtained from the NF-to-FF transformation, including the magnitude and phase of the estimated far-field pattern.
- (8) Must: Generate elevation cuts of the magnitude from the far-field results.
- (9) Additional: Execute the transformation using experimental data points.
- (10) Additional: Deliver spherical grid scan configuration.
- (11) Additional: Use time-gating to filter out reflections.

1.5 Context of the Project & Distribution of Tasks

This section describes the context of the project and the division of the project among the different groups.

The project forms the main component of the Bachelor Graduation Project (Bachelor afstudeer project, BAP) of eight Electrical Engineering Bachelor students at the TU Delft. To respond to today's limitation in flexibility in scanning geometries, the THz sensing group at the TU Delft decided to invest in a promising measurement method based on the automated robotic arm. The project that this BAP group will undertake is to build atop the initial research conducted by this department, to automate the antenna measurements.

The bachelor graduation project is divided into four groups of two students. The distribution of tasks is presented below.

Subgroup 1 is responsible for the automation of the robotic arm. They ensure that the robot moves smooth and follows user-specified measurement patterns (theta-phi, Ludwig II, Ludwig III). In addition, subgroup 1 optimizes the path for the robotic arm to minimize large rotation of the robot's joints.

Subgroup 2 presents the User-Interface and incorporates the work of all four subgroups. They are tasked to join and synchronize all the parts in this project. Additionally, subgroup 2 is conducting and analysing tests to identify potential phase errors introduced by the movement or positioning of the robot arm during measurements.

Subgroup 3 develops the acquisition algorithm for a far field spherical scan. Measuring the 3D antenna radiation pattern over a spherical surface is important to characterize the total radiated power and the antenna directivity. The most point efficient far-field grids are studied, including Fibonacci grid and Gauss-Legendre grid.

This paper covers the part of the project completed by **subgroup 4**. The objective of subgroup 4 is to estimate the far-field radiation pattern and the according directivity of the AUT, based on near-field measurements. The developed program has to be generic to accommodate arbitrary scanning geometries. The motivation and objective is explained in depth in the introduction, Section 1.

1.6 Outline of Thesis

This report is divided into six main sections.

Section 2: *Basic Antenna Theory* gives the reader the foundational knowledge of the developed program.

Section 3: *Methodology* provides a clear, detailed, and replicable description of the design process. First, the complete system to be simulated is introduced. Then, the design steps are explained, each building on the previous ones and increasing the complexity.

Section 4: *Program Structure & Functionality* describes the practical implementation of the steps outlined in section 2, along with additional features.

Section 5: *CST simulations* explains how CST simulations were used to cross validate the design

process.

Section 6: *Results and Validation* analyses the obtained results and compares them with the expected results. Eventual discrepancies are identified and explained.

2 Basic Antenna Theory

Near-Field region and Far-Field region

According to [2, Section 2.2.4], the definition for far-field and near-field regions is : *"The space surrounding an antenna is usually subdivided into three regions: reactive near-field, radiating near-field (Fresnel) and far-field (Fraunhofer) regions as shown in Figure 3. These regions are so designated to identify the field structure in each. Although no abrupt changes in the field configurations are noted as the boundaries are crossed, there are distinct differences among them. The boundaries separating these regions are not unique, although various criteria have been established and are commonly used to identify the regions."* Within the scope of our project, the radiated near-field, abbreviated with *near-field* or NF, and the *far-field*, abbreviated with FF are of concern. The NF region is defined within

$$0.62\sqrt{D^3/\lambda} < R < 2D^2/\lambda \quad (1)$$

where λ is the wavelength, R is the distance between antenna and point of observation, D is the largest side of the aperture for a rectangular aperture, or the diameter of the aperture, both in meter. The separation distance between the NF grid and the origin will henceforth be called NF distance. The far field region is taken to exist when the NF regions stop. For those equations to be valid D must also be larger than the wavelength ($D > \lambda$).

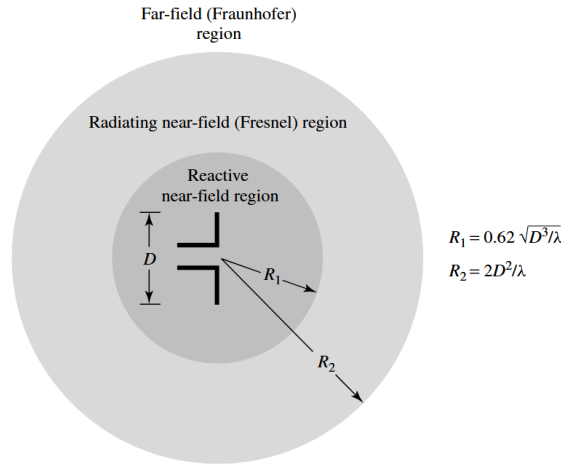


Figure 3: Field regions of an antenna.[2, Section 2.2.4]

Equivalence theorem

An intuitive technique used to estimate the FF radiation using NF measurements is the equivalence theorem [6], [7]. As [6, p.648] puts it *"The radiated fields can be computed with the help of the field equivalence principle, which states that the aperture fields may be replaced by equivalent electric and magnetic surface currents."* In practice, this means a measurement grid is created in the NF of the AUT and at each node of the grid a short dipole are simulated whose radiation is related to the

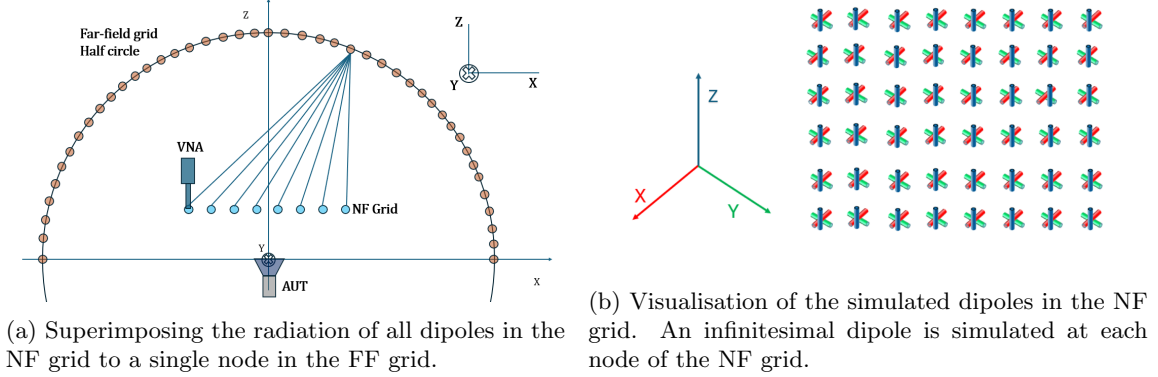


Figure 4: Representation of the equivalence theorem.

radiation of the AUT at that node, in the measured direction (2). This process is repeated until the full E-field is captured.

$$\mathbf{E}_{\text{AUT}} = E_0 \hat{p} \propto S_{12} \hat{p} \propto I_{\text{dipole}} \hat{p} \quad (2)$$

The E-field of all the dipoles in the measurement grid are projected onto another grid in the FF of the AUT. The summation of all the E-fields from the dipoles estimate the radiated FF from the actual AUT. Figure 4a attempts to showcase part of the equivalence theorem.

Validity angle

Ideally, the NF measurement grid would infinitely large, capturing the complete NF radiation pattern. This is not practical as it would mean infinitely many measurement points. The limited size has two consequences. First, as can be seen in Figure 5, it limits the validity region of the estimation of the FF. The validity region is defined by the validity angle. The equation for the validity angle is the following

$$\theta_v = \arctan \left(\frac{L - a}{2d} \right) \quad (3)$$

where θ_v is the validity angle in radians, a is the AUT longest side, L is the length of the side of the NF grid parallel to a , d is the separation distance between the AUT aperture and the measurement plane. Note that the validity angle is only an approximation and not a strong definition. Second, the discontinuities at the edges of the measurement plane introduce error in the valid region. [16] As the author [5, Section 19.3.2.2] puts it: *To determine whether the scan area is large enough, we set the data in the outer perimeter of the scan area to zero and observe how much the computed far field changes. As a rule of thumb, the scan area should be large enough so that measurements, at the edges, are at least 30 dB below (and preferably 40 dB or more below) the near-field peak.*

Co-polarization & cross-polarization

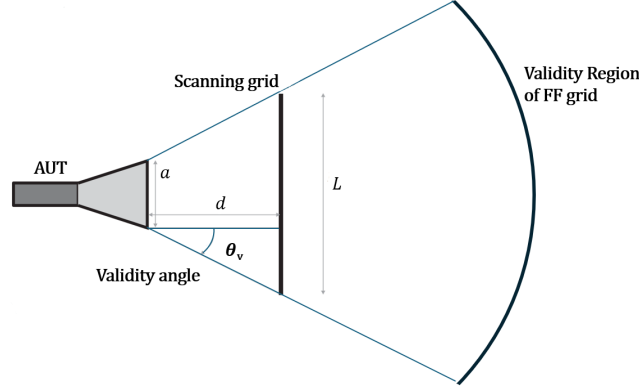


Figure 5: FF grid limited by validity angle. Adapted from [5, Section 19.3.2.2].

Antenna polarization exists due to the fact that all EM energy travels in the form of a 2-Dimensional wave. Antennas are designed in such a way that the radiation and so-called polarization of the energy, mainly stored in the electric-field, are mathematically or empirically known, enabling efficient transmission and reception of wireless signals. The intended polarization of an antenna is called the co-polarization.

As the actual polarization does not exactly match the intended theoretical polarization, a small part of the energy is lost in the so-called cross polarization. For example, a lens antenna propagating along the z-axis, parallel to the x- and y-axis radiates a planar E-field. The intended co-polarization could be along the x-axis, the amount of E-field that would be along y is then in cross-polarized, undesired. Different antennas have different radiation geometries and polarizations. We want to be able to mathematically model those polarizations. This is what the three Ludwig definitions achieve. A more in depth description of polarization can be found in [2, Section 2.12], [17], [18]

Ludwig's polarization definitions

Arthur C. Ludwig presented in 1973 three geometrical definitions for mathematical representations of co- and cross polarization along a sphere [17] [19]. Ludwig's third definition will be the main concern of this report. Ludwig's third definition gives the two mathematical equations to define the co- and cross polarization of an antenna located at the origin, radiating along the positive z-axis, with the co-polarization being along the y-axis. The equation tracks both polarizations as the observation points shifts from the centre.

$$co-pol.(\theta, \phi) = \sin(\phi)E_{\theta} + \cos(\phi)E_{\phi} \quad (4)$$

$$Cross-pol.(\theta, \phi) = \cos(\phi)E_{\theta} - \sin(\phi)E_{\phi} \quad (5)$$

Vertical polarization and horizontal polarization

Vertical polarization and horizontal polarization are new replacement names for co- and cross polarization when the user does not know which orientation is co or cross i.e. when the antenna is

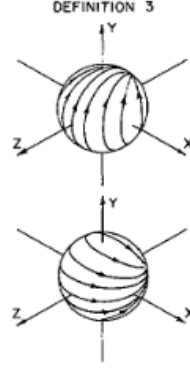


Figure 6: Visualisation of Ludwig 3 definition, from [17].

rotated 90° , co-polarization becomes cross-polarization. By renaming them horizontal- and vertical-polarization, the name simply tells the orientation of the polarization, and not whether they are co- or cross.

Directivity

The directivity is an important parameter of an antenna. The directivity measures the degree to which the radiation is concentrated in a single direction, relative to the radiation intensity averaged over all directions. At first the radiation intensity, $R^2 S_{av}(r, \theta, \phi) = U(\theta, \phi)$ is calculated in Eq.6.

$$U(\theta, \phi) = \frac{1}{2\zeta} |E_0(\theta, \phi)|^2 \quad (6)$$

Then the radiation power is found by integrating radiation intensity over the entire solid angle, by Eq.7 and finally the directivity can be calculated by Eq.8.[20, Sec.9-2.3]

$$P_{rad} = \iint U(\theta, \phi) \sin(\theta) d\theta d\phi \quad (7)$$

$$D_0 = \frac{4\pi U_{max}}{P_{rad}} \quad (8)$$

3 Methodology

The objective of our work is to estimate the FF of the AUT using measurements made in the NF region of the antenna. The ensemble of measurements is called *NF grid*, *measurement grid*, *scanning grid* and *scanning geometries* interchangeably. In order to successfully complete our program, it must be developed through multiple progressive steps, where each step increases the project in complexity and is intended to validate a certain set of functions and equations. The motivation behind each step is explained in its corresponding section.

3.1 Definition of Reference System & Grids

A schematic overview of the whole system can be seen in Figure 7.

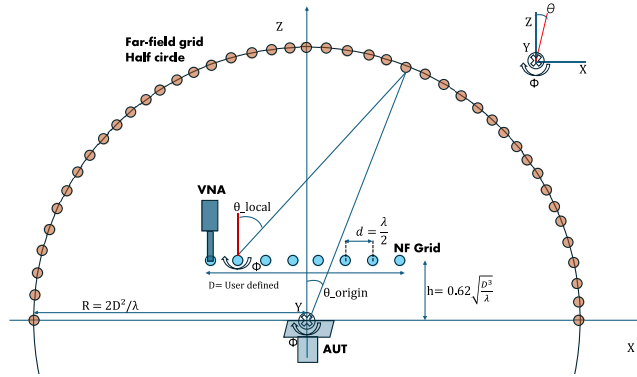


Figure 7: Schematic overview of entire setup - Visualisation of difference between θ from a node in NF grid to a node in the FF grid, and θ from the origin to the same node in the FF grid.

Defining Reference system

The system uses right-handed Cartesian and spherical coordinate system. r , θ and ϕ are defined according to Figure 8.

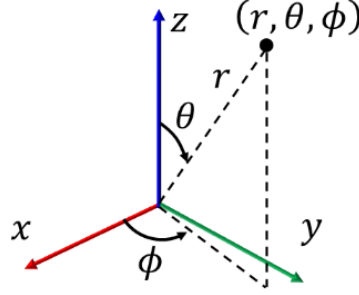


Figure 8: Cartesian and Spherical coordinate systems used.

The centre of the aperture of the AUT is then placed at the origin of the reference system, radiating along the positive z-axis.

Defining the Near-Field Grid

A planar measurement grid is simulated in the NF of the antenna. As the AUT will always be placed to radiate along the +z axis, the measurement grid will always be in the +z region of the Cartesian coordinate system, aligned with the central axis of the antenna. The distance of the NF grid is chosen according to the Eq. 1. To ensure the valid region is maximized, the distance is set at the lower boundary. The NF grid can also be tilted along theta with respect to the AUT placed in the origin.

The dimensions of the grid in meters (referred to by 'NF dimensions'), the distance between the AUT and NF grid in meters (referred to by 'NF distance') and the tilt of the NF grid in degrees are defined by the user. The maximal spacing d between the evenly spaced nodes [5, Section 19.3.2.2] is fixed at

$$d = \frac{\lambda}{2} \quad (9)$$

Defining the Far-Field Grid

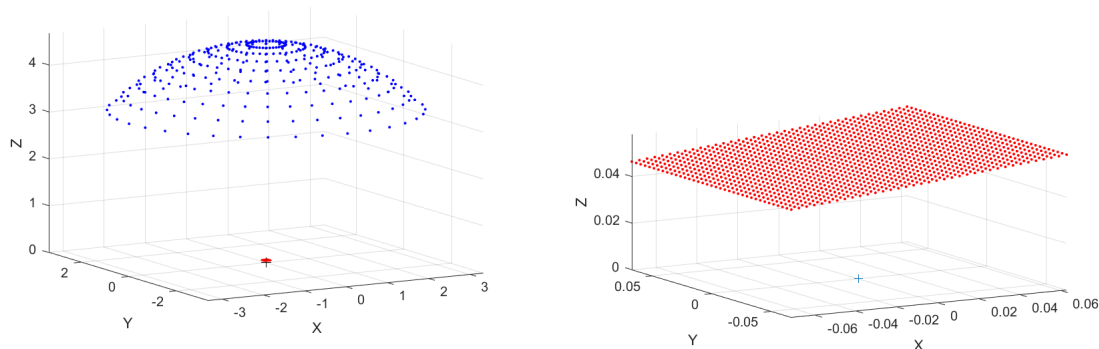
An equiangular, half-spherical FF grid is placed centred in the origin. It is defined with θ and ϕ , ranging between $[0^\circ, 90^\circ]$ and $[0^\circ, 360^\circ]$ respectively. The FF grid has a minimal radius of

$$R = \frac{2D^2}{\lambda} \quad (10)$$

where D is the diameter of the aperture in meters, or the largest side of a rectangular aperture. In the case of the NF-to-FF transformation, D is redefined as the largest side of the NF grid, as the NF grid is behaving like an aperture of an antenna.

When the NF to FF transformation is performed, θ of the FF grid is capped by the validity angle, whilst ϕ is kept in the range $[0^\circ, 360^\circ]$.

The amount of nodes between the nodes is fixed at 360 and 91 for ϕ and, θ respectively. This is to ensure sufficient FF data points, numerical estimation of the analytical radiation. The simulated fields are plotted in Fig.9.



(a) Complete system: downsampled Far-field grid (blue), near-field grid (red) and location of AUT (+). FF capped at validity angle.

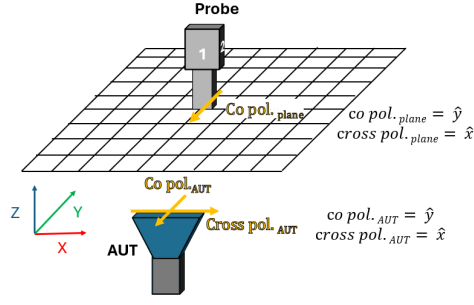
(b) Close up on near-field grid (red) and AUT (+).

Figure 9: View of the complete system and close-up on the NF grid.

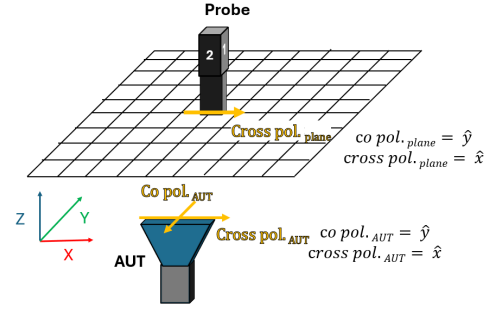
Polarization of Measurements and Simulated Dipoles

Please refer to Figure 10 while reading this Section. In order to get an accurate representation of the radiation of an antenna, both co- and cross polarization have to be measured (Sec.2). This means that the VNA measures the E-field two times at each point: once for each polarization, indicated as horizontal and vertical polarization. Following that logic, two perpendicular dipoles aligned with the directions of the polarizations are simulated at each node. One for each polarization, each with their own current. Note that measuring the E-field is done by aligning the probe with the desired polarization (Figure 11b). To simplify the system by keeping the direction of the polarizations simple, the AUT can only be placed with co-polarization along the x- or y-axis. This limits the direction of polarization to either x or y direction, see Figure 11a. Therefore, for an untilted plane, dipoles only have to be simulated along the x- and y-axis.

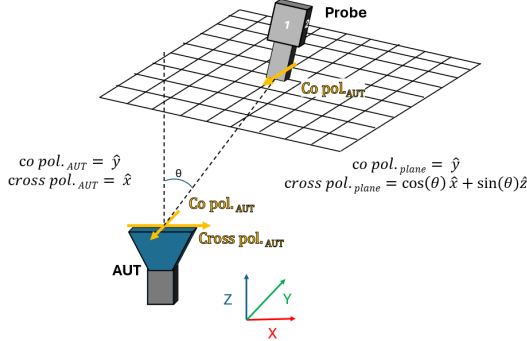
However, the objective is to keep the program flexible to arbitrary scanning geometries: in the case of a tilted or spherical grid, the direction of the co and cross polar of the grid may no longer be purely along x- and y any more, but along x, y and z simultaneously. In other words, the E-field is no longer only along x or y any more (Figures 10a10b, but also along z (Figures 10c10d. For those cases, a dipole along z also has to be simulated. All three dipoles along x, y and z are always simulated to keep the program constant and robust, even if the E-field may not be along z (Figure 4b).



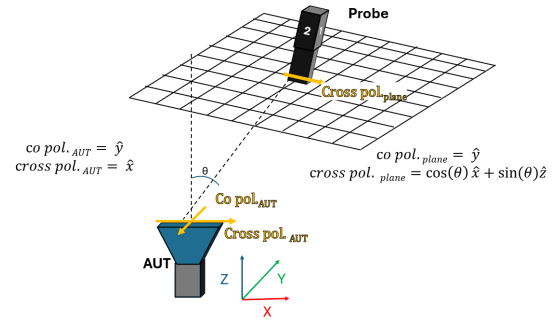
(a) Measurement of the co pol. of the antenna for a scanning grid parallel to XY plane (untilted).



(b) Measurement of the cross pol. of the antenna for a scanning grid parallel to XY plane (untilted).

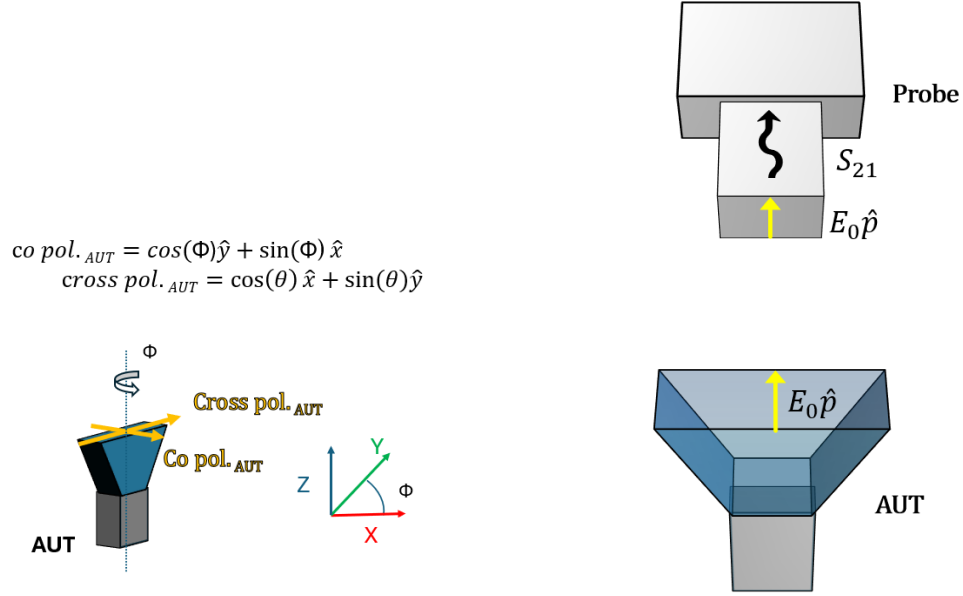


(c) Measurement of the co pol. of the antenna for a scanning grid tilted along θ .



(d) Measurement of the cross pol. of the antenna for a scanning grid tilted along θ .

Figure 10: Visualising how the tilted plane affects the direction of the co pol. and cross pol. vectors.



(a) Direction of polarizations if AUT not aligned with x and y axis. (b) Radiation from the antenna is picked up by the probe in the same orientation.

Figure 11: Importance of orientation of the antenna and the probe.

3.2 Validation steps

This section explains the validation steps used to validate the program, Figure 12 summarises these steps with their objective.

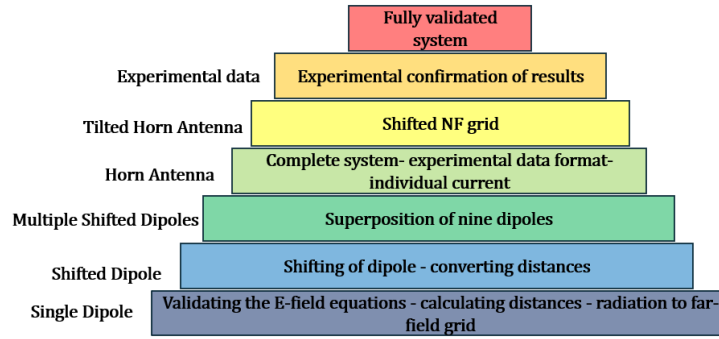


Figure 12: The validation steps, with their objective, completing each other to form a functional system.

3.2.1 Single Dipole at the Origin

The FF grid is created at the beginning of each simulation as described in 3.1. Unless specified otherwise, the radius of the FF grid is 1 metre.

A single dipole along x, y and z, at the origin and is radiated onto each node of the far-field at 10 GHz. Figure 20b represents a sketch of a single dipole oriented along x. The dipoles oriented along y and z are positioned in similar fashion. This step is intended to validate the equations that lie at the base of the program. This includes 1) Calculating the rectangular and spherical distances between the dipole and each node of the FF grid. 2) The equations of the radiated E-field from a short dipole along x, y and z. 3) The value of the E-field at each node of the FF grid. Below are the equations for the radiated E-field of an infinitesimal dipole.

Equation for the radiated E-field from an infinitesimal dipole along the z-axis at the origin.

$$\mathbf{E} \approx I_{\text{dipole}} \frac{jk\zeta l}{4\pi r} e^{-jkr} \sin(\theta) \hat{\theta} \quad (11)$$

Equation for the radiated E-field from an infinitesimal dipole along the x-axis at the origin.

$$\mathbf{E} \approx I_{\text{dipole}} \frac{jk\zeta l}{4\pi r} e^{-jkr} (-\cos(\theta) \cos(\phi) \hat{\theta} + \sin(\phi) \hat{\phi}) \quad (12)$$

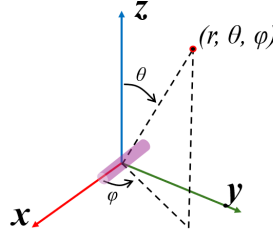


Figure 13: Short dipole oriented along x direction.

Equation for the radiated E-field from an infinitesimal dipole along the y-axis at the origin.

$$\mathbf{E} \approx I_{\text{dipole}} \frac{jk\zeta l}{4\pi r} e^{-jkr} (-\cos(\theta) \sin(\phi) \hat{\theta} + \cos(\phi) \hat{\phi}) \quad (13)$$

where $k = 2\pi/\lambda$ [$\frac{1}{m}$], $\zeta = 120\pi$ [Ω], $I=1$ [A] and $l = \lambda/50$ [m], are the wave number, the characteristic impedance of vacuum, the current through the dipole and the length of the diode respectively. r , θ and ϕ are calculated using the following formulas.

$$r = \sqrt{x^2 + y^2 + z^2} \quad (14)$$

$$\theta = \arccos\left(\frac{z}{r}\right) \quad (15)$$

$$\phi = \arctan\left(\frac{y}{x}\right) \quad (16)$$

where x , y and z represent the rectangular distances between the dipole and a point in the FF grid.

3.2.2 Single Dipole Shifted by 5 cm

A single dipole along x , shifted by 5 cm from the origin in the positive x direction, is simulated at 10 GHz and radiated onto the FF grid. Figure 7 helps to understand the following key statement. The equations of the E-field given above are in terms of r , θ and ϕ . These values represent the distance between the dipole and the observation point in spherical coordinates (spherical distance). The spherical distances between point A and point C are different from the spherical distances between point B and C. If the distances are different, the E-field components along θ and ϕ will also be different. As the goal is to estimate the E-field radiated from the AUT (at the origin), the E-field of the shifted dipole has to be converted to be with respect to the origin, rather than its own location. To this effect, vector coordinate conversion is applied. First, the E-field is converted from being composed of E_θ , E_ϕ , E_r , for r , θ and ϕ with respect to the location of the shifted dipole, to E_x , E_y , E_z . Afterwards, E_x , E_y , E_z are converted to E_θ , E_ϕ , E_r , for r , θ and ϕ with respect to the origin. The goal of this step is to validate this conversion.

3.2.3 Dipole Grid

Multiple, shifted dipoles are simulated at 10GHz and radiated onto the far field grid. It is important that the spacing between each dipole and its closest neighbours is at most $\lambda/2$, see Fig. 14. The purpose of this step is to superimpose the radiation from multiple dipoles to get the total E-field at a FF node. The same vector coordinate conversion from the shifted dipole is applied here, with a slight adjustment: E_x , E_y , E_z of each dipole are now summed up before the last conversion step.

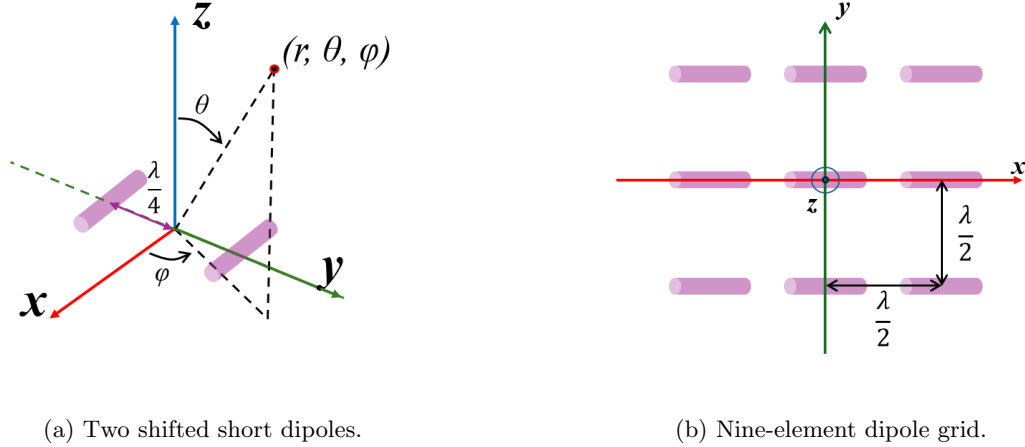


Figure 14: Multiple shifted dipole configurations.

3.2.4 Normal Oriented Horn Antenna at Origin

The WR28 horn antenna [21] is simulated at 30 GHz in CST Sec.5. The antenna located at the origin radiates along the $+z$ axis, see Fig. 15a, where the direction of the co-pol is along the y -axis. The E-field from the horn antenna is ‘sampled’ in CST and exported to MATLAB. The sampling grid is 140 mm by 140 mm and centred at the origin. The points are spaced by 5 mm, which means the grid is oversampled as $5 \text{ mm} = 0.005 \text{ m} < \lambda/2 = 0.02 \text{ m}$. The grid has 784 sampling points.

This stage is mostly a repetition of the previous step, but with 784 dipoles instead of 9, and with the grid being at 30 mm from the XY plane. It is the first simulation of the complete system, as it is the first time an antenna is sampled in the NF and the data points are passed through the transformation program. This also implicates that each dipole has its own current, Eq. (2). In the previous steps, all dipoles had 1 A current. The goal of this step is to validate the complete system, which means the base requirements of the project are met. This step is also used to integrate the data format in which the experimental data will be supplied.

3.2.5 Tilted Horn Antenna at Origin

The WR28 horn antenna is simulated at 30GHz in CST at the origin, with $\theta = 15$ and $\phi = 0$, see Fig. 15b, with the co-pol of the antenna being along y -axis. Consequently, the NF grid also has to be tilted by that same amount. The objective of this step is to validate the concept of polarization of the measurements, explained at the end of Section 3.1.

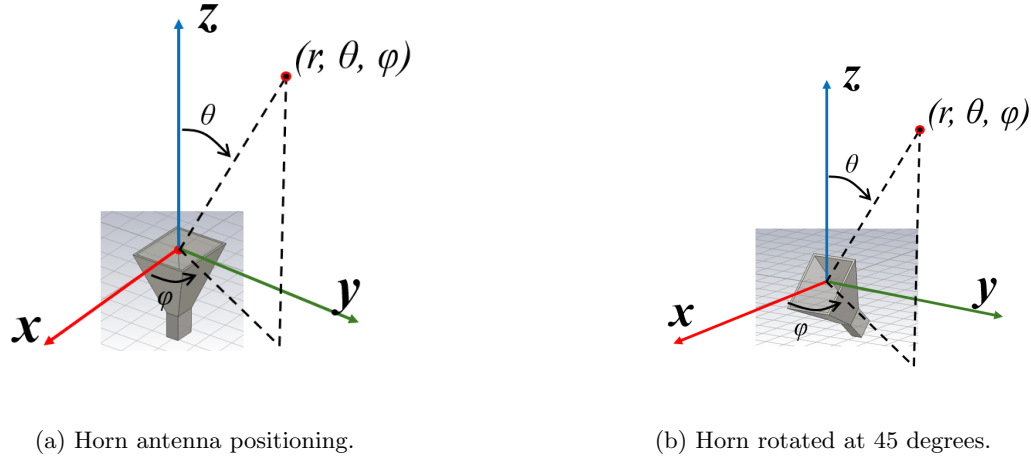


Figure 15: Horn antenna position and orientation.

3.2.6 Experimental Validation

In this case the WR28 horn antenna is measured in real world. The setup is similar of how it is described in Sec.3.2.4 and in Sec.3.2.5. The goal of this step is to validate the integration of all different subgroups, Section 1.5, into a fully functional system. Then the results are compared with the results from CST.

Normal Oriented Horn

The normal oriented horn configuration is placed according to the Fig.15a. More detailed sketch about the dimensions of the NF grid for the measurements can be seen in Figure 16. The sketch is done implying the validity angle of 45 degrees and a minimal NF distance at maximum sweep frequency. Those values also behave as input parameters to the graphical user interface (GUI) from subgroup 2. Figure 17a shows a picture from the lab where the measurements were performed. After the measurements subgroup 2, export the results in format specified in Sec. 4.2, after which the data is processed and can be compared to CST.

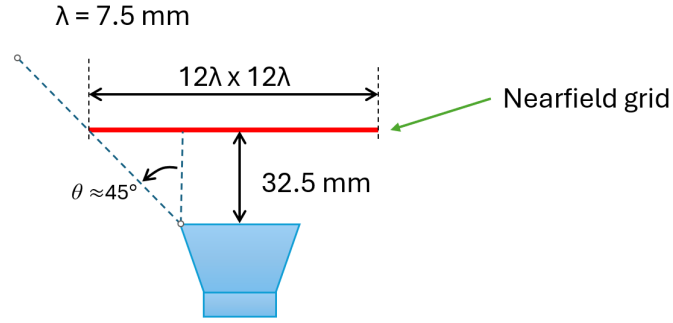
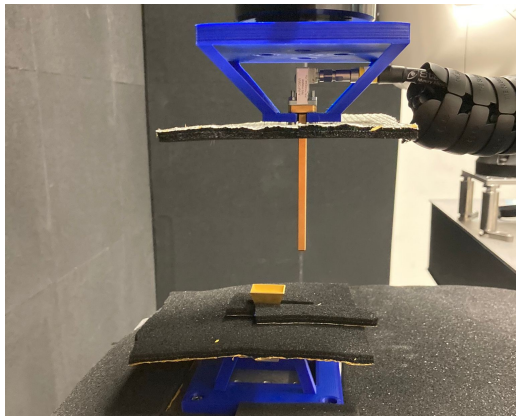


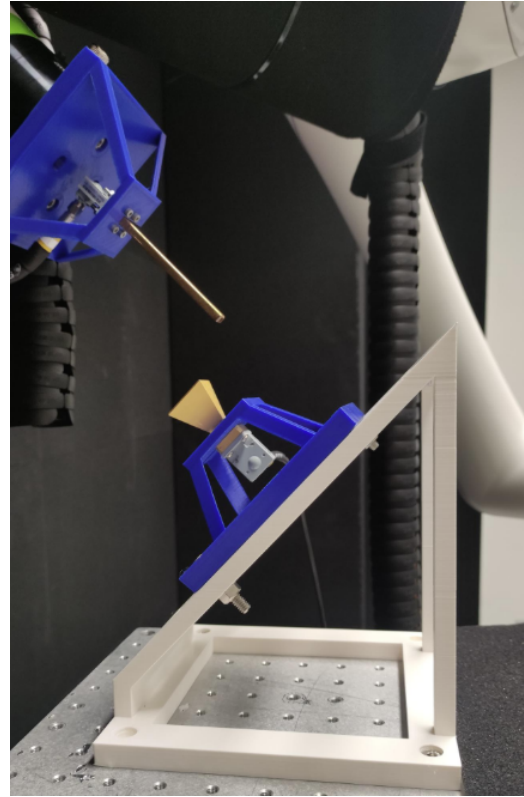
Figure 16: Normal oriented horn setup sketch.

Tilted Horn

The normal oriented setup is then rotated and measured at an angle of 45° (Fig. 17b), where it is placed in the same fashion as in Fig.15b. This is needed to test the functionality of our MATLAB script under the titled scenario. For the sake of testing the developed algorithms, the scanning is synthesized by physically rotating the antenna. In practice, this could represent the case of a planar array that scans the beam away from broadside.



(a) Horn setup for NF measurement.



(b) Tilted horn setup for NF measurement.

Figure 17: Horn setups during experimentation.

3.3 Obtaining the Directivity

The directivity can be calculated after completion of the transformation algorithm. To calculate the directivity, the NF measurements are extracted for a single frequency and transformed to the far field. The directivity for that frequency is then calculated from the FF pattern according to Equation 8. This process is repeated for each frequency, resulting in a directivity versus frequency figure.

3.4 Plotting Results

The most convenient way to validate results is to visualise them. Magnitude and phase of the E-field are of main interest. Two kinds of plots are used in this report: UV plots and cuts. Those plots will be used to examine the magnitude of the absolute E-field, the magnitude of the co and cross polarization, and the phase of the co and cross polarization.

3.4.1 UV Plots

UV plots are a useful way to transform the 3D half-spherical vector field into a 2D planar surface, using colour to represent either magnitude or phase. UV plots offer an overview of the results and serve as the first visual validation of the results. UV plots of the magnitude of the E-field are expressed in dB and normalized individually to their own maximum value - MATLAB and CST are normalized individually. These plots are also limited to -40dB. UV plots of the phase of the E-field are expressed in degrees and wrapped in the range $[-180^\circ, 180^\circ]$. They are normalized relative to the phase at $\theta = 0, \phi = 0$. Whilst the plotting boundaries for magnitude and phase are different, they both use the same colour scale.

3.4.2 Cuts of the Magnitude

Magnitude cuts provide a clearer view of specific values and help spot differences between MATLAB results and CST validation. Four cuts are shown, each for θ ranging from 0° to 90° and ϕ fixed. These cuts are included:

- Co polarization: $\phi = 0^\circ, 45^\circ$ and 90° .
- Cross polarization: $\phi = 45^\circ$

As with the UV plots, the magnitude is normalized to its own maximal value.

4 Program Structure & Functionality

This section guides the reader through the main called upon functions in the MATLAB program, while explaining the philosophy behind them. The names of functions are written in the **typewriter font**, the names of data structures and variables are written in *italic* to repeatedly clarify the difference between the two.

4.1 Setting Up & Viewing the Grids

The user first defines the parameters of his system in the GUI made by group 2, see Section 1.5. (frequency, aperture size, NF distance, size of the NF grid, tilt angle NF grid) The parameters are then inputted in a function called `verifyInputs.m` where the NF grid, the capped FF grid and the antenna at the origin are plotted in the same figure (see Figure 9a). The goal of that figure is to give the user a representation of the set-up (relative placement and size of NF grid, FF grid and antenna wrt each other) and give him the chance to adapt parameters before running the measurements.

As the FF grid is much larger than the NF grid, inspecting the NF grid can be challenging, therefore the NF grid is also plotted alone to more precisely visualise the locations of the measurement points and an eventual tilt (Figure 9b). Some extra information is also outputted to the user, such as the value of the validity angle, whether the NF grid is located in the NF region of the antenna, and whether the condition from Section 2, $D < \lambda$ holds.

This is explained in more detail below.

4.1.1 Implementing the Near-Field Grid

The planar NF grid, largely defined by the user, is created by the `createNFgrid.m` function. The NF dimensions, the NF distance and the tilt angle of the NF grid are user-defined. The spacing between the points is fixed at $\lambda/2$

Some features are implemented to help the user satisfy the antenna theory explained in Section 2.

- If the separation distance between the NF grid and the AUT is not inside the range defined by Eq. 1, then the user is notified of this problem.
- Tilting the NF grid can place some measurement points below $z=0$. Those points below $z=0$ would be below the AUT and therefore not of interest. To avoid measuring meaningless points, the user gets to either discard those points or redefine his measurement grid. The problematic points may even be below the table on which the antenna is placed, in which case it is crucial to discard those points in order to avoid damaging the probe and robotic arm.
- Measuring the radiation properties of an antenna may require sampling at different frequencies. However, the grid has to be kept constant at all frequencies while satisfying the antenna theory, at all frequencies. By choosing the highest frequency to set the spacing in the NF grid, the maximal spacing between nodes is satisfied at all frequencies tested.

The errors introduced in the valid area by discontinuities (Section 2) are not yet taken into account by the program.

4.1.2 Implementing the far-field grid

The `createFFgrid.m` function is called subsequently to `createNFgrid.m`. The user does not have direct decision power in defining the FF grid, he can indirectly influence it by changing NF dimensions or the frequency.

As with the NF grid, the grid has to be kept constant at all frequencies while satisfying the antenna theory. Therefore, the radius is defined with the highest frequency measured at, see Eq. 10. Furthermore, θ of the FF grid is set equal to the validity angle, as depicted by Figure 9a. The errors introduced in the valid area by discontinuities (Section 2) are not yet taken into account by the program.

If the user is satisfied with the grids, he can choose to start the measurement. Please refer to the reports of subgroup 1 and 2 for further information.

4.2 Storing and Transferring the Measured Data

The measured data is received in a `.mat` file, this is a MATLAB-specific data file. The `.mat` file contains one `struct`, `meas_data`, that contains all the information needed to estimate the far-field pattern. Figure 18 provides a clear summary of the contents of `meas_data`.

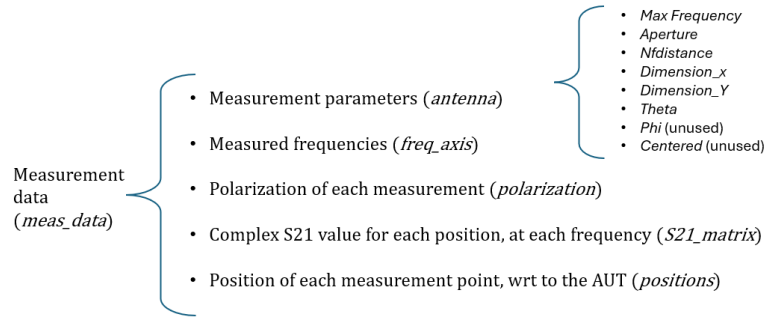


Figure 18: Format of received measurements data.

As explained in Section 3.1, the direction polarization of the antenna measurements may be divided along the x, y and z-axes when using tilted or spherical grids, see Figure 10. For this reason, the measured E-field must always be decomposed along the x, y and z axis so that simulating 3 dipoles along those axes always captures the full 3D direction of the E-field, see Figure 4b.

The `get_measurements_data` function goes through received the data struct, `meas_data`, and extracts the relevant data to convert to 6 outputted lists; x position, y position and z position; and E_x , E_y and E_z . The raw data has now been extracted and put into more manageable lists. Each complete data point can be reconstructed by taking the element at the same index from all six lists.

`measurement_data` takes the long lists of data points and groups them in a cell array called `data_cells`. Each cell of the `data_cells` cell array is a list. Each list summarises all the information needed to simulate a dipole at a specific location in five floats. The 5 elements of the list are [x-position, y-position, z-position, orientation of the dipole (1= along x, 2= along y, 3= along z),

current through the dipole in corresponding orientation]. This list of 5 elements shall henceforth be called ‘a complete dipole’. Equation 17 shows the structure of *data_cells*.

$$\begin{aligned} \text{multidipoles} = \{ & [x_0, y_0, z_0, 1, I(pol.)], \\ & [x_0, y_0, z_0, 2, I(pol.)], \\ & [x_0, y_0, z_0, 3, I(pol.)], \\ & [x_1, y_0, z_0, 1, I(pol.)], \\ & [x_1, y_0, z_0, 2, I(pol.)], \\ & [x_1, y_0, z_0, 3, I(pol.)], \\ & \dots, \\ & \text{complete dipole}[n] \\ & \} \end{aligned} \tag{17}$$

The S21 parameter is directly inputted as the dipole current, according to Equation 2. Note that for 100 measurements points in the NF grid, 200 measurements are taken (co and cross), and 300 dipoles are simulated along x,y and z).

4.3 Simulating & superimposing the dipole E-fields

The NF measurements, converted to lists summarising all information needed in *data_cells*, are now ready to be transformed to form the FF radiation pattern. The transformation is done within 2 functions: *dipoleContributions.m* and *multiDipole.m*. Remember that each *complete dipole* contains the location, orientation and current of the dipole along that orientation. *dipoleContributions.m* extensively uses those values.

DipoleContribution.m calculates the E-field radiated by one complete dipole to each point of the FF grid. To accomplish this, the function requires one complete dipole and the FF grid coordinates as inputs parameters. The following enumerations summarises in a clear and concise manner the steps undertaken in *dipoleContributions.m*.

1. The function first uses the dipole’s location to calculate the x, y and z distance of the given dipole to each point of the FF grid. The rectangular distances are then transformed to spherical positions, relative to the position of the dipole (see Section 3.2.2 and Figure 7).
2. The E-field of the dipole at each point of the FF grid is calculated using one of the E-field equations of a dipole (Equations 12, 13, 11). Which one is used is defined by the fourth element of a *complete_dipole* list.
3. The infinitesimal dipole is excited by the current given in the fifth element of the *complete_dipole* list.
4. *DipoleContributions* outputs E_x , E_y and E_z from inputted dipole to all the points in the FF grid.

mulitDipole.m goes through each *complete dipole* and superimposes the E-fields from each to form the far-field pattern. To achieve this, *mulitDipole.m* requires the complete *data_cells* variable. Each *complete dipole* is passed through *DipoleContributions.m* and the outputted E-field

from `DipoleContributions.m` are summed up. When this is done, the resulting $E_{x,total}$, $E_{y,total}$, $E_{z,total}$ are converted to E_r , E_θ , E_ϕ where θ and ϕ are defined wrt to the origin of the reference system (Section 3.2.2).

Lastly, the co and cross polarizations are calculated according to equations 4 and 5.

4.4 Directivity

Two functions are created. 1) `directivity.m`: this function takes as input the absolute, total E-field as well as r , θ and ϕ and outputs the directivity in dBi, according to Section 2. 2) `get_directivity.m` performs the NF-to-FF transformation for each calls out the main function which calculated the far-field for each of the frequencies of interest and displays the figure for frequency versus directivity.

4.5 Plotting

Different figures can be requested by the user:

- A figure containing three UV plots: the magnitude of the far-field radiation pattern of the AUT field, the co and the cross polarization of the E-field.
- A figure containing two UV plots: the phase of the far-field radiation pattern of the AUT field, the vertical and the horizontal polarization of the E-field.
- A figure containing four cuts for θ 0 to 90° of the magnitude of the far-field radiation pattern of the AUT. Cuts of the magnitude of the co-polarization at ϕ 0°, 45° and 90° and a cut of the magnitude of the cross-polarization at ϕ 45°. The magnitudes are normalized with themselves.
- A figure containing four cuts for θ 0 to 90° of the phase of the far-field radiation pattern of the AUT. Cuts of the phase of the co-polarization at ϕ 0°, 45° and 90° and a cut of the phase of the cross-polarization at ϕ 45°.
- A figure containing two plots of the magnitude of the measured near-field E-field. The plots display the magnitude of the co-polarization and the cross polarization of the measured near-field E-field.
- A figure containing two plots of the phase of the measured near-field E-field. The plots display the phase of the co-polarization and the cross polarization of the measured near-field E-field.
- A figure containing a plot of the directivity versus frequency. The plot displays the selection of frequencies at which the measurements were performed. And

All 6 figures are provided for a NF-to-FF estimation, which corresponds to the last methodology steps: plotting the near-field of a dipole does not make much sense as that step does not involve any near-field yet.

5 CST Simulation

Progress of our MATLAB script has to be validated at every step, which makes debugging easier and makes our program more reliable. To this effect, CST Studio Suite 2020 is used to create reliable simulations of dipoles and antennas, and cross validate them with the results obtained from MATLAB. The following section explains how the reader may recreate the CST simulations used to validate the obtained results.

5.1 Environment Setup

After opening CST, the user can create a *New Template*, which simplifies the environment setup: choose *Microwaves & RF/Optical - Antennas, Waveguide, Time Domain*, default *Units*. In *Settings* choose *Frequency range* from 8 to 12 GHz, *Monitors*: E-field and far-field defined at 10 GHz. The user should have a similar *summary* as displayed in Figure 19. The described environment will be used for dipole simulations. After the project has been set, the user can start by modelling the short dipole.

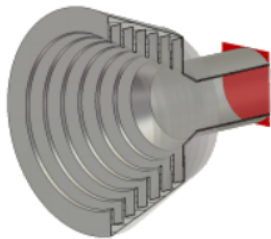
Create Project Template

MW & RF & OPTICAL | Antennas | Waveguide (Horn, Cone, etc.) | Solvers | Units | Settings | **Summary**

Please review your choice and click 'Finish' to create the template:

Template Name:

Antenna - Waveguide_3



Solver



Time Domain

Units

- Dimensions: mm
- Frequency: GHz
- Time: ns
- Temperature: Kelvin

Settings

- Frequency Min.: 8 GHz
- Frequency Max.: 12 GHz
- Monitors: E-field, Farfield
- Define at: 10 GHz

Antennas which consist of waveguide elements or which transform energy from guided form (waveguide, coaxial line) to radiating by a gradual transition, e.g. horn or conical elements.

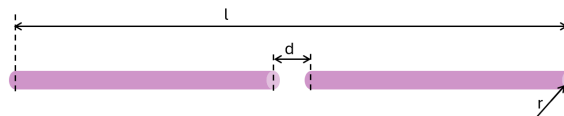
Figure 19: CST project template summary used for dipole simulations.

5.2 Dipole Simulations

Start by defining the parameter list used in the simulation (Fig. 20) for the sketch of the dipole. In the modelling tab, select *cylinder* and define it with the filled in parameters. Also, select the perfect electric conductor (PEC) material for the cylinder. To separate the dipole rods, create a box and define it in the origin with the dimension d . Remove the box with the boolean operator *subtract*. Afterwards, assign discrete ports on the inner circles of the dipole sides. The dipole model is complete. Simulate it by using the time domain solver.

Parameter List				
	Name	Expression	Value /	Description
---	r	= l/100	0.006	radius antenna
---	d	= l/20	0.03	distance between rods
---	l	= lambda/50	0.6	length antenna
---	fc	= 10	10	Frequency in GHz
---	lambda	= 300/fc	30	Wavelength

(a) Parameters used for dipole.



(b) Dipole sketch with dimensions

Figure 20: Simulated dipole with according parameters.

5.3 Export Setting and Post-processing

After simulation, the resulting far-field has to be exported. The settings of the far-field plot are described in Appendix C.1, Fig. 61. After setting the plot parameters, go to the *Far-field Plot* tab and select *Result templates*. These settings can be seen in Appendix C.1, Fig. 62. After the evaluation of the results, a *.txt*-file is created. The file is then processed by MATLAB to calculate horizontal and vertical polarization defined by Ludwig-3, and the UV plots of the magnitude and phase and the magnitude cuts are displayed. The output of which can be seen in the Appendix C.2.

5.4 Other Dipole Configurations

New dipole configurations can be achieved with some slight modifications.

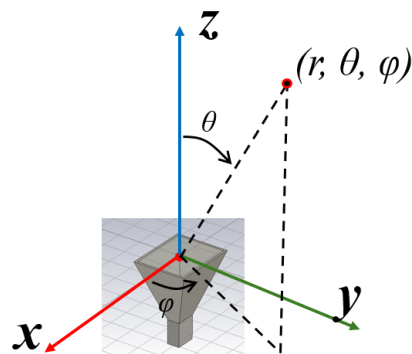
To avoid losing the results from previous CST simulations, use the *save as* option and save the single dipole simulation.

The *Transform* tool, along with the *Rotate* and *Shift* functions, can be used to create different configurations of dipoles. The export settings and procedure to follow when updating the configuration are the same for every simulation.

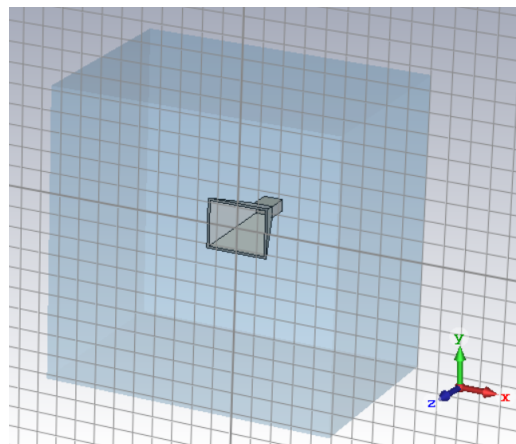
5.5 Horn Simulation

For the horn simulation, create a new project template and select the *Frequency range* simulation to be from 26GHz to 41GHz. The frequencies the user wants to monitor, can be selected for the creation of the field monitor. And for the horn simulation, the far-field export settings stay the same.

The model of the horn can now be created or imported. Consult the datasheet [21] for the dimensions



(a) Horn positioning and orientation.



(b) Model of horn antenna in CST with vacuum box around.

Figure 21: Horn antenna in CST simulations.

of the model of the horn antenna. Use Fig.21a to position and orient the antenna. After the model of the horn antenna is complete, set the waveguide port, through which the signal will be passed, to the base of the horn antenna. To export the near-field data, a box has to be created around the horn antenna with the material properties of vacuum. The dimensions of the box have to be such that the box is fully in the NF region (Fig. 21b). Also, the E-field monitor has to be added to the simulation environment to be able to export the NF data. Use the time domain simulator and run it.

After the simulation is completed, export the far-field using the same settings as before. To export the near-field, go to *2D/3D Results* and select E-field with the desired frequency. Then go to the *Result Templates* and choose export 3D results, for specific settings advice the Appendix C.3.

5.6 Rotated Horn Antenna at Origin

No simulation could be finalised for a rotated horn antenna, as the CST simulation required more RAM than our computers had (50GB). However, our MATLAB program has to be validated with the tilted near-field data. So, the NF data from the previous simulations is rotated around the origin by the wanted amount by reusing our *rotate.m* function. The far-field on the other hand can be exported by changing the reference system of plot properties, see Appendix C.4.

6 Results & validation

In order to verify the veracity of our simulations, each case described in Section 3 is cross validated with an identical CST simulation. Validation is done visually by comparing the UV plots and the cuts of the MATLAB and CST simulation. The build up in complexity of the cases allows for a smoother validation process.

To avoid overcrowding the report, most figures are placed in the appendix and referenced to. However, important takeaways from the results and potential differences are explained in the corresponding section below.

6.1 Single Dipole at the origin

A single dipole along x, y and z at the origin is simulated. The comparison between the MATLAB results and CST validation for all three dipoles are depicted in Appendix Section B.1. All three orientations show the expected results: the magnitude of the E-field of an infinitesimal dipole on a half-sphere. Furthermore, the UV plot of the magnitudes and cuts of the magnitude show a perfect match between MATLAB and CST. However, the phase plots show a near symmetry of the phase. This symmetry has likely been introduced by differences in assumptions between CST and MATLAB simulations. Time constraints didn't allow us to fully discover the underlying difference. The phase differences can be seen both in the UV plot of the phase and a single cut at $\phi = 45$. Besides the phase difference, both magnitude and phase are almost identical in MATLAB versus CST. The first validation step has been completed.

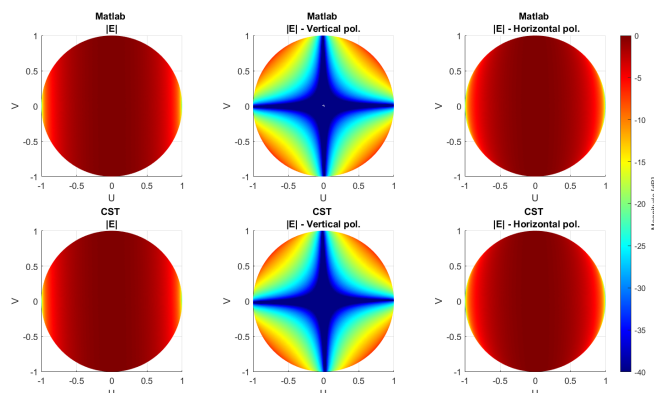


Figure 22: UV plot of the magnitude of the E-field on the FF grid of a dipole along x, located at the origin.

6.2 Single dipole along X, shifted by 5 cm

A single dipole along X, shifted by 5 cm from the origin in the positive x direction, is simulated. Simulating dipoles along Y and Z has been validated, therefore those simulations won't validate anything the dipole along X won't. The results are in Appendix Section B.4. Once again, the magnitude is nearly identical in MATLAB and CST. The phase symmetry is still, the symmetric aspect can be better observed in the phase cut included in the section. Besides the phase difference,

both magnitude and phase are almost identical in MATLAB versus CST. The second validation step has been completed.

6.3 Dipole Grid

A 3 by 3 grid of dipoles along X, spaced by $\lambda/2$ centred at the origin, is simulated. The results can be seen in the Appendix Section B.5. The magnitudes match very well once again. The general aspect of the phase still matches, however additional discrepancies appear at every multiple of $\phi = 45$. Besides the phase difference, both magnitude and phase are almost identical in MATLAB versus CST. The third validation step has been completed.

6.4 Horn antenna at the origin

The WR28 horn antenna is simulated at the origin, radiating in the positive z-direction, with the direction of the co pol. along the y-axis. The results can be seen in the Appendix B.6. The main lobe and the side lobes are recognized in the MATLAB results. The general aspect of the magnitude and the shape are nearly identical, except for the phase symmetry. At very low magnitudes, as is the case in the cross-pol plot (horizontal polarization), phase errors are amplified as a small change in one of the complex components of the E-field may result in large phase changes. The measured magnitude and phase at the NF grid are also shown. At the end of the section, the UV plots of the magnitude and phase capped by the validity angle are shown.

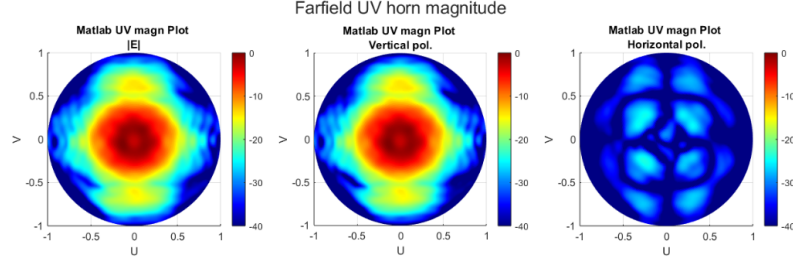
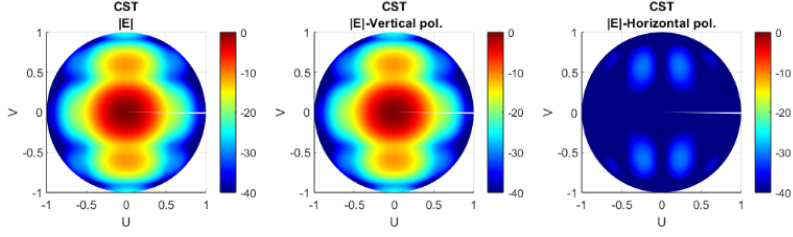
6.5 Tilted horn antenna at the origin

The same horn antenna as in the previous step is simulated, only now the antenna is tilted by 15° along the x-axis. The results can be seen in the Appendix Section B.7. Again, the main lobe and the side lobes are clearly visible, only tilted. The phase plot of the cross-pol looks different from the CST simulation. This is due to the E-field being very small and variations having a big impact on the phase, as explained for the case of the horn at the origin. Notice that the plots seem to be rotated by $\phi = 90$, this is due to the fact that the CST simulation of a rotated horn did not work for reasons beyond our power (excessive RAM usage). Therefore, to validate the addition of the tilt to the program, the sampled data for a normally oriented horn at the origin from the previous case is tilted. During the tilting, the data was undesirably changed as the radiation pattern seems to be rotated along $\phi = 90$. This means the tilting ability of the grid could not be properly validated, but as the previous results are promising, and the error is beyond our control, this step is considered as validated.

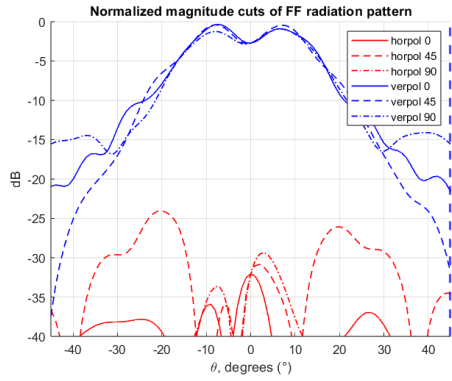
6.6 Experimental Validation

6.6.1 Normal Oriented Horn antenna at the origin

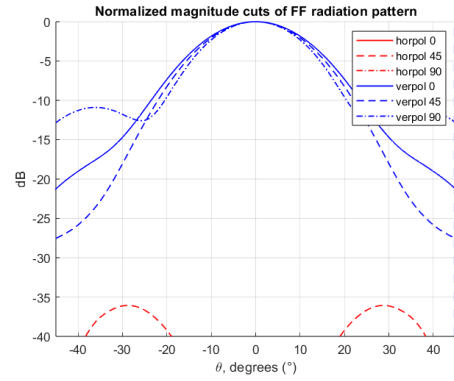
Using the setup described in Sec. 3.2.6(Normal Oriented Horn) measurements are performed. The resulting S21-parameters are then exported and processed by our MATLAB script. The following results are achieved and compared to the CST simulation results. Beside that the remaining figures can be found in Appendix B.9. The Fig.23 the vertical polarization shows strong resemblance in the validity region. In the horizontal polarization case, strong influence of reflection is present which result in higher magnitude at cross-pol.

(a) Measured far-field magnitude of $z+$ oriented horn [dB].(b) Simulated far-field magnitude of $z+$ oriented horn [dB].Figure 23: Comparison of measured and simulated far-field magnitude UV plots of $z+$ oriented horn.

For some more comparative result the magnitude cuts are compared, see Fig. 24. As one can observe the measured farfield has a distinct dip of about 3dB at $\theta = 0$. This could be due to reflections between the probe and antenna.



(a) Measured horn far-field cuts (NFtoFF-transformed).

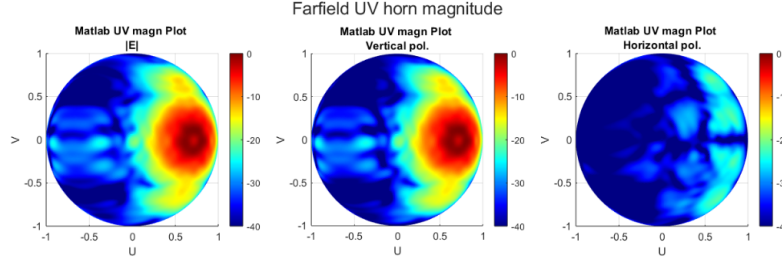


(b) Simulated horn far-field cuts (CST).

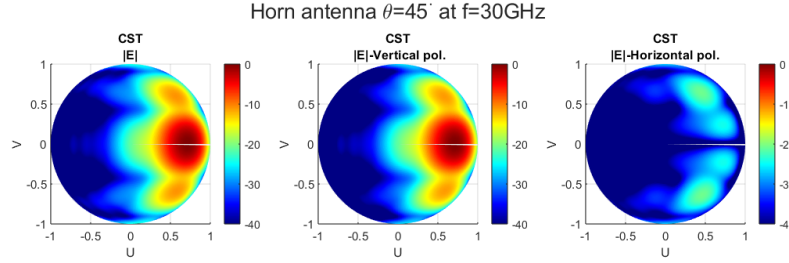
Figure 24: Comparison of measured and simulated far-field magnitude cuts of $z+$ oriented horn.

6.6.2 Tilted horn antenna at the origin

For the tilted case the measurements were performed with the setup described in Sec. 3.2.6(Tilted Horn). The UV plot representation comparison can be seen in Fig. 25. As one can observe the similar 3dB dip can be seen at the maximum radiation of the antenna.



(a) Measured far-field magnitude of 45 degree oriented horn [dB].



(b) Simulated far-field magnitude of 45 degree oriented horn [degree].

Figure 25: Comparison of measured and simulated far-field magnitude UV plots of 45 degree oriented horn.

6.6.3 Directivity

When the FF is estimated from the experimental measurements, the directivity can be calculated and compared to the simulated results. In Fig. 26 the results can be seen. The error is quite substantial, resulting in 1-2 dBi difference. This might be due to the invalid region in the FF plot.

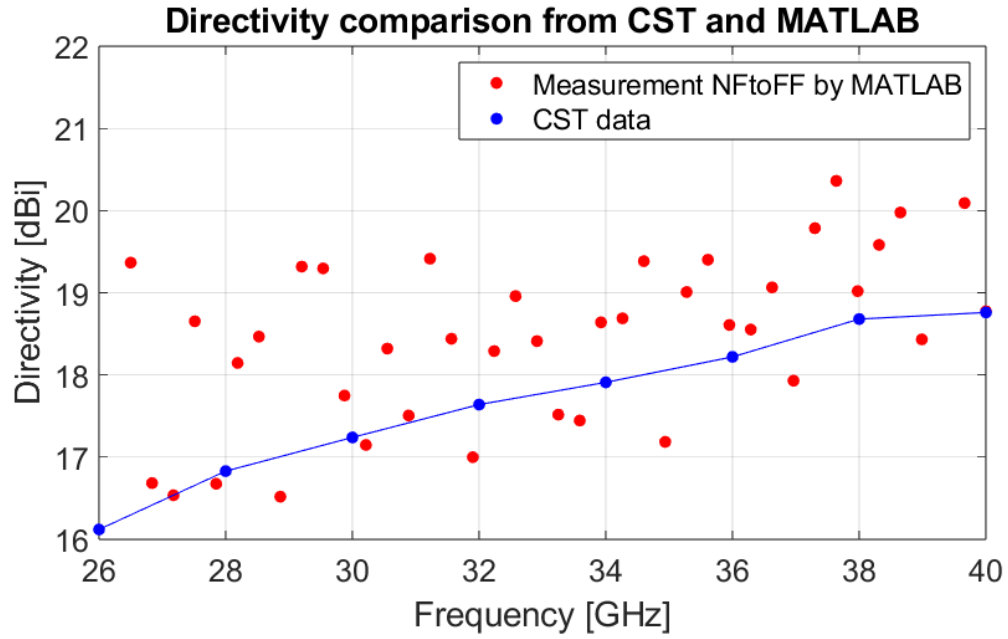


Figure 26: Comparison of directivity from real-world NF measurements and CST of horn WR28 antenna.

7 Summary, Discussion & future work

7.1 Summary

The aim of our work was to extend conventional planar measurement grids by enabling measurements over an arbitrary spatial surface, through the use of a 6-axis robotic arm. Such computer-controlled robotic arm also provides high accuracy and high repeatability of the movement pattern. A vector network analyser (VNA) is placed at the extremity of the 6-axis robotic arm.

The separation distance between the antenna under test (AUT) and the far-field can exceed the reach of the robotic arm. In such cases, the far-field must be estimated using near-field measurements. This near-field to far-field transformation is achieved by applying the equivalence theorem Section 2.

The transformation process was implemented through a series of MATLAB functions. The initial step focusses on verifying the equations that form the foundation of the program, such as distance calculations, E-field radiation from an infinitesimal dipole, and radiation pattern computations. These were confirmed through simulations of a single dipole aligned along the x-, y-, and z-axes at the origin, as discussed in Section 3.2.1.

Subsequent validation steps expanded the program and tested the robustness of the transformation under different configurations. A single dipole along x, y and z was shifted 5 cm along the x-axis to confirm proper conversion between relative spherical angles (Section 3.2.2). Superposition of fields was verified using a 3×3 dipole array spaced by $\lambda/2$ to confirm correct field summation, (Section 3.2.3).

The complete system was then validated using CST simulations of a horn antenna. The E-field was sampled in CST according to the NF grid and exported to MATLAB in the data format intended for experimental data (Section 3.2.4). A rotated horn antenna was also tested to evaluate performance on a tilted measurement surface (Section 3.2.5). These steps confirmed that the system meets the basic requirements. Finally, actual measurement data was used to repeat the last two validation steps, and the resulting FF pattern from the transformation was compared with results from CST. All validation steps were completed successfully, except for a minor symmetry effect observed in the phase figures.

7.2 Discussion & Future Work

Our work lays a strong foundation for implementing a NF to FF transformation using an automated robotic arm. However, can be expanded and enhanced in many ways. While our work is complete, it lacks the implementation of more advanced NF-to-FF transformation methods and, more importantly, the validation of diverse scanning grids, the central motivation behind our project. Furthermore, positioning errors of the robotic arm should be taken into account.

With respect to our work, areas of improvements remain to be explored:

- Correcting the phase symmetry between the CST and MATLAB results

- A study on the interpolation errors between the discrete amount of far-field nodes, and subsequent improvement of the standard equiangular far-field grid.
- A study on the errors introduced by the equivalence theorem as transformation method, and the errors in the validity region caused by discontinuities at the edges of the NF grid.
- A study on the inaccuracies in the estimation due to positioning errors of the robot.[8]
- A study on the influence of the probe on the results. [22] [23]
- An implementation of time gating technique on measured S-parameters to mitigate the influence of reflections.

To conclude, the near-field to far-field transformation method has been successfully implemented. While the project offers many opportunities for improvement, it establishes a solid foundation. Further development of the project will significantly improve the antenna research.

Bibliography

- [1] K. Wolfgang and E. Gillespie, “Antenna Measurements,” IEEE proceedings, vol. 66, no. 4, Apr. 1978.
- [2] C. A. Balanis, *Antenna theory: analysis and design - Elektronische Ressource*, en, 3. ed. Hoboken, N.J: Wiley-Interscience, 2005, ISBN: 978-0-471-66782-7.
- [3] M. Meng, A. Wu, Z. Stokesberry, T. Zhao, S. Y. Lee, and N. Ghalichechian, “Robotic Radiation Pattern Measurement System for 6–110 GHz Based in Both Near Field and Far Field,” in *2023 IEEE International Opportunity Research Scholars Symposium (ORSS)*, Atlanta, GA, USA: IEEE, Apr. 2023, pp. 11–15, ISBN: 979-8-3503-3700-6. DOI: 10.1109/ORSS58323.2023.10161734. [Online]. Available: <https://ieeexplore.ieee.org/document/10161734/> (visited on 06/15/2025).
- [4] ElMaReCo, Copenhagen, Denmark, O. Breinbjerg, M. Sierra Castañer, *et al.*, “Antenna Measurement Challenges and Opportunities,” en, *Reviews of Electromagnetics*, vol. 2, pp. 1–49, Dec. 2023, ISSN: 27094057. DOI: 10.53792/roe/2023/23003. [Online]. Available: <https://www.euraap.org/roe-vol2-23003> (visited on 06/12/2025).
- [5] M. H. Francis and R. C. Wittmann, “Near-Field Scanning Measurements: Theory and Practice,” en, in *Modern Antenna Handbook*, C. A. Balanis, Ed., 1st ed., Wiley, Aug. 2008, pp. 929–976, ISBN: 978-0-470-03634-1 978-0-470-29415-4. DOI: 10.1002/9780470294154.ch19. [Online]. Available: <https://onlinelibrary.wiley.com/doi/10.1002/9780470294154.ch19> (visited on 04/25/2025).
- [6] S. J. Orfanidis, “Ch. 14 - Radiation fields,” en, in *Electromagnetic waves & Antennas*, ECE Rutgers University, 2008, ISBN: 978-0-9793713-2-5. [Online]. Available: www.ece.rutgers.edu/~orfanidi/ewa.
- [7] R. Johnson, H. Ecker, and J. Hollis, “Determination of far-field antenna patterns from near-field measurements,” en, *Proceedings of the IEEE*, vol. 61, no. 12, pp. 1668–1694, 1973, ISSN: 0018-9219. DOI: 10.1109/PROC.1973.9358. [Online]. Available: <http://ieeexplore.ieee.org/document/1451288/> (visited on 04/25/2025).
- [8] P. F. Wilson, J. A. Gordon, D. R. Novotny, and J. R. Guerrieri, “Antenna metrology for 100–500 GHz: A new approach,” in *2016 Asia-Pacific International Symposium on Electromagnetic Compatibility (AP EMC)*, Shenzhen, China: IEEE, May 2016, pp. 909–911, ISBN: 978-1-4673-9494-9. DOI: 10.1109/AP EMC.2016.7522904. [Online]. Available: <http://ieeexplore.ieee.org/document/7522904/> (visited on 06/15/2025).
- [9] D. Novotny, J. Gordon, J. Coder, M. Francis, and J. Guerrieri, “Performance evaluation of a robotically controlled millimeter-wave near-field pattern range at the NIST,” en, 2013.
- [10] J. A. Gordon, D. R. Novotny, M. H. Francis, *et al.*, “Millimeter-Wave Near-Field Measurements Using Coordinated Robotics,” en, *IEEE Transactions on Antennas and Propagation*, vol. 63, no. 12, pp. 5351–5362, Dec. 2015, ISSN: 0018-926X, 1558-2221. DOI: 10.1109/TAP.2015.2496110. [Online]. Available: <http://ieeexplore.ieee.org/document/7312446/> (visited on 06/14/2025).
- [11] H. Jansen and D. Heberling, “Numerical Analysis of Positioning Errors in Irregular Near-Field Antenna Measurements Using Robot-Based Systems,” en,

- [12] B. L. Moser, J. A. Gordon, and A. J. Petruska, “Increased Efficiency in Planar Near-Field Scanning Using Combined Multi-Robot Motion,” en,
- [13] S. F. Gregson and C. G. Parini, “Use of Compressive Sensing Techniques for the Rapid Production Test of Commercial Nose-Mounted Radomes in a Robotic Antenna Measurement System,” en,
- [14] A. Husein, K. Rasilainen, J.-P. Makela, A. Parssinen, and M. E. Leinonen, “6G OTA Measurements at Sub-THz Band Using a Compact Robotic System,” en,
- [15] S. Gregson, C. Parini, D. Lewis, and W. Cooper, “A comparison of near-field to far-field transformation techniques for use with industrial multi-axis robotic antenna measurement systems,” en, *International Journal of Microwave and Wireless Technologies*, pp. 1–10, Feb. 2025, ISSN: 1759-0787, 1759-0795. DOI: 10.1017/S1759078725000157. [Online]. Available: https://www.cambridge.org/core/product/identifier/S1759078725000157/type/journal_article (visited on 04/28/2025).
- [16] Arthur D. Yaghjian, *Upper-Bound Errors in Far-Field Antenna Parameters Determined From Planar Near-Field Measurements* (NBS technical note 667). National Bureau of Standards, Oct. 1975.
- [17] A. Ludwig, “The definition of cross polarization,” en, *IEEE Transactions on Antennas and Propagation*, vol. 21, no. 1, pp. 116–119, Jan. 1973, ISSN: 0018-926X, 1558-2221. DOI: 10.1109/TAP.1973.1140406. [Online]. Available: <https://ieeexplore.ieee.org/document/1140406/> (visited on 06/14/2025).
- [18] R. Kumar Jaiswal, R. Kumar Dutta, S. Bhattacharya, C.-Y.-D. Sim, and K. V. Srivastava, “Study on Co-and Cross-Polarization Radiation Patterns of Dipole Antenna,” en, in *2023 IEEE International Symposium on Antennas and Propagation and USNC-URSI Radio Science Meeting (USNC-URSI)*, Portland, OR, USA: IEEE, Jul. 2023, pp. 1321–1322, ISBN: 978-1-6654-4228-2. DOI: 10.1109/USNC-URSI52151.2023.10237945. [Online]. Available: <https://ieeexplore.ieee.org/document/10237945/> (visited on 05/14/2025).
- [19] J. Roy and L. Shafai, “Generalization of the Ludwig-3 definition for linear copolarization and cross polarization,” en, *IEEE Transactions on Antennas and Propagation*, vol. 49, no. 6, pp. 1006–1010, Jun. 2001, ISSN: 0018926X. DOI: 10.1109/8.931162. [Online]. Available: <http://ieeexplore.ieee.org/document/931162/> (visited on 06/14/2025).
- [20] F. T. Ulaby and U. Ravaioli, *Fundamentals of applied electromagnetics*, en, 7th ed. Boston: Pearson, 2015, ISBN: 978-0-13-335681-6 978-1-292-08244-8.
- [21] *WR-28 Pyramidal Horn Antenna*, 2023. [Online]. Available: <https://sftp.eravant.com/content/datasheets/SAR-1725-28-S2.pdf>.
- [22] E. Joy, W. Leach, and G. Rodrigue, “Applications of probe-compensated near-field measurements,” en, *IEEE Transactions on Antennas and Propagation*, vol. 26, no. 3, pp. 379–389, May 1978, ISSN: 0096-1973. DOI: 10.1109/TAP.1978.1141856. [Online]. Available: <http://ieeexplore.ieee.org/document/1141856/> (visited on 04/25/2025).
- [23] D. Paris, W. Leach, and E. Joy, “Basic theory of probe-compensated near-field measurements,” en, *IEEE Transactions on Antennas and Propagation*, vol. 26, no. 3, pp. 373–379, May 1978, ISSN: 0096-1973. DOI: 10.1109/TAP.1978.1141855. [Online]. Available: <http://ieeexplore.ieee.org/document/1141855/> (visited on 04/25/2025).

- [24] M. Samsuzzaman and M. T. Islam, “Inverted S-Shaped Compact Antenna for X-Band Applications,” en, *The Scientific World Journal*, vol. 2014, pp. 1–11, 2014, ISSN: 2356-6140, 1537-744X. DOI: 10.1155/2014/604375. [Online]. Available: <http://www.hindawi.com/journals/tswj/2014/604375/> (visited on 06/14/2025).

A Appendix

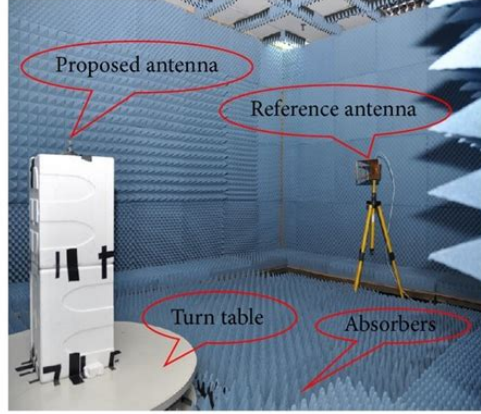


Figure 27: Measurement set-up with fixed spherical scanning grid.[24]

Generic equation for the radiated E-field from an infinitesimal dipole at the origin.

$$\mathbf{E} \approx \frac{-j\omega\mu Il}{4\pi r} e^{-jkr} ((p_x \cos(\theta) \cos(\phi) + p_y \cos(\theta) \sin(\phi) - p_z \sin(\theta)) \hat{\theta} + (-p_x \sin(\phi) + p_y \cos(\phi)) \hat{\phi}) \quad (18)$$

B MATLAB results

B.1 Single dipole at origin along X

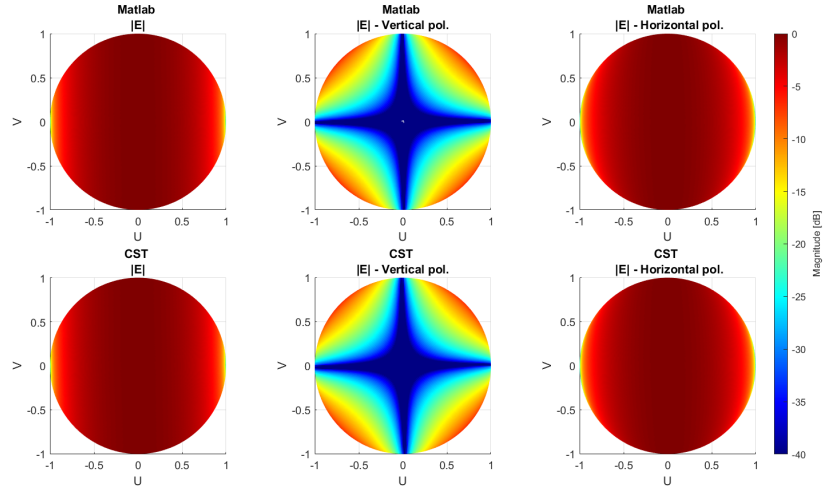


Figure 28: UV plots comparing the magnitude of a dipole at the origin along X, simulated in MATLAB (above) vs a dipole simulated in CST (below).

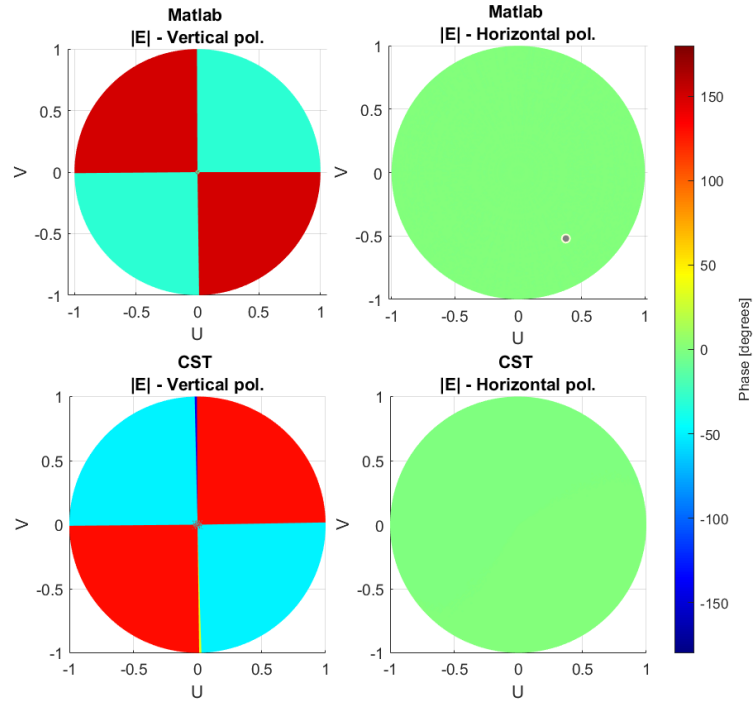


Figure 29: UV plots comparing the phase of a dipole at the origin along X, simulated in MATLAB (above) vs a dipole simulated in CST (below).

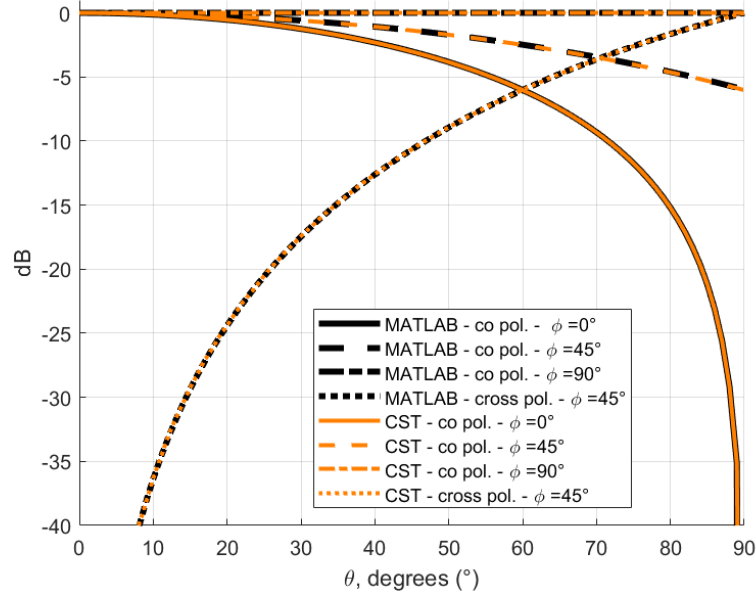


Figure 30: Magnitude cuts comparing the magnitude of a dipole at the origin along X, simulated in MATLAB (black) vs a dipole simulated in CST (orange).

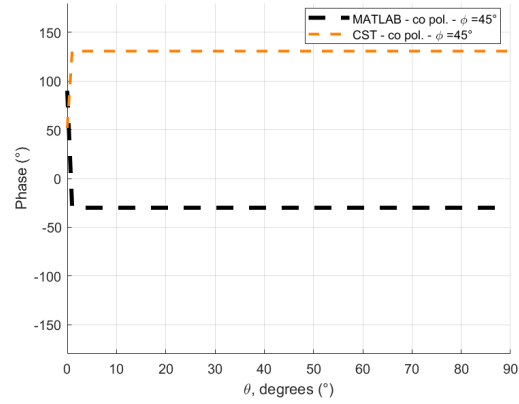


Figure 31: Single Phase cut comparing the phase of a dipole at the origin along X, simulated in MATLAB (black) vs a dipole simulated in CST (orange).

B.2 Single dipole at origin along Y

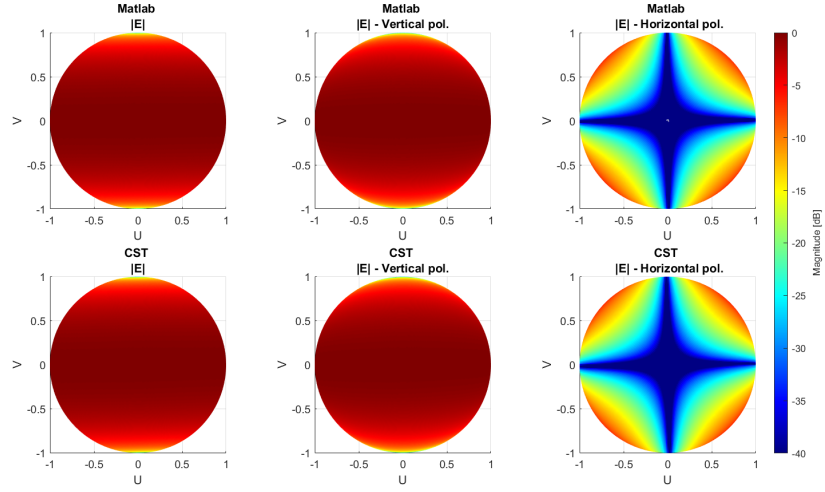


Figure 32: UV plots comparing the magnitude of a dipole at the origin along Y, simulated in MATLAB (above) vs a dipole simulated in CST (below). .

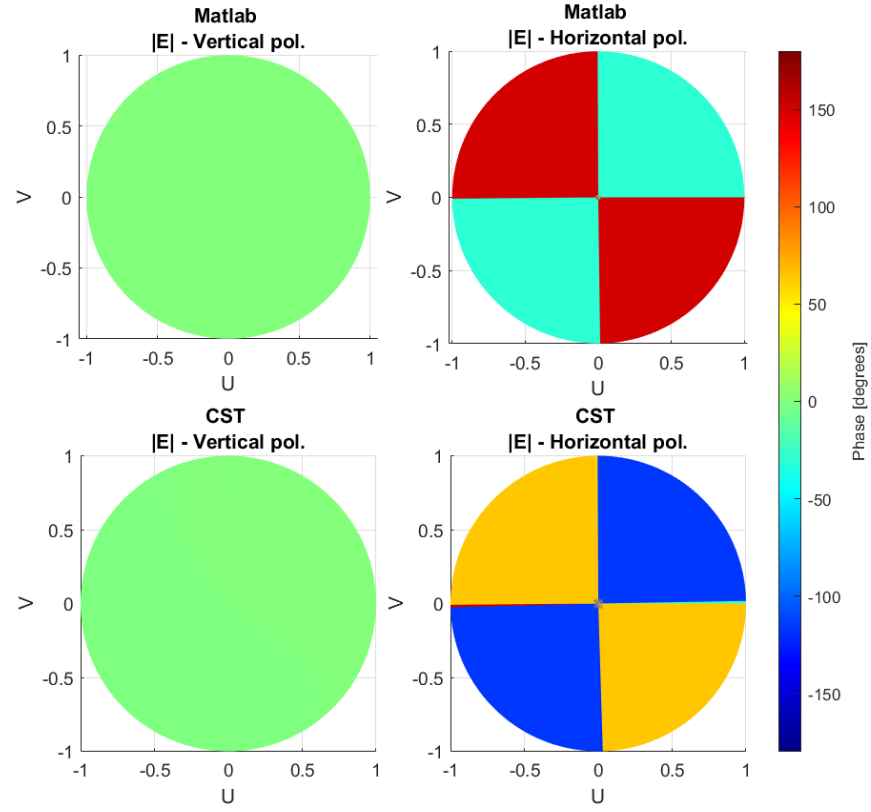


Figure 33: UV plots comparing the phase of a dipole at the origin along Y, simulated in MATLAB (above) vs a dipole simulated in CST (below).

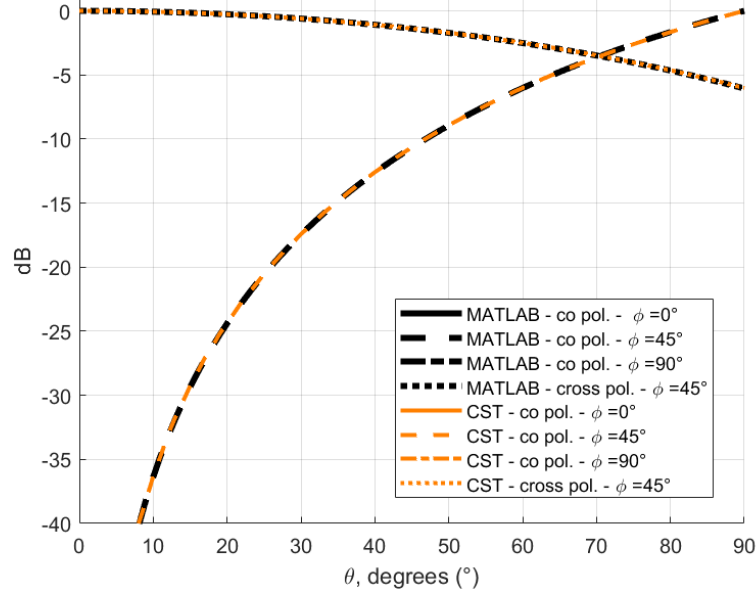


Figure 34: Magnitude cuts comparing the phase of a dipole at the origin along Y, simulated in MATLAB (black) vs a dipole simulated in CST (orange).

B.3 Single dipole at origin along Z

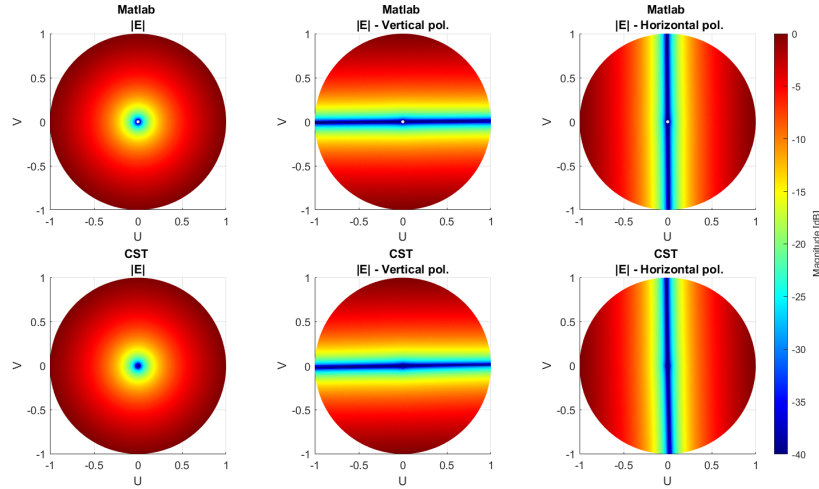


Figure 35: UV plots comparing the magnitude of a dipole at the origin along Z, simulated in MATLAB (above) vs a dipole simulated in CST (below).

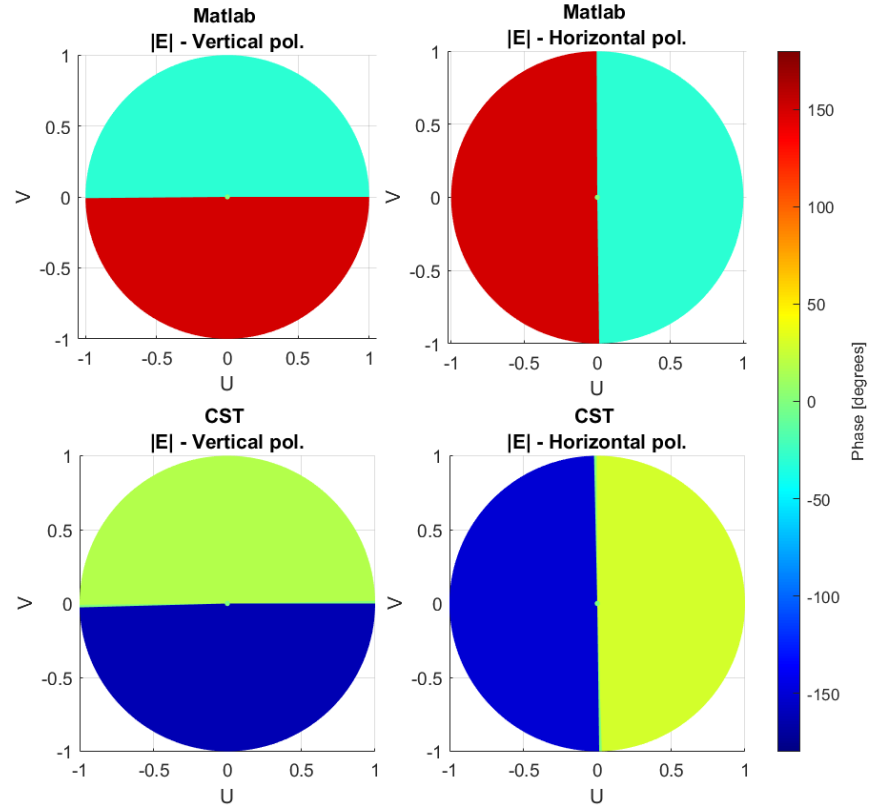


Figure 36: UV plots comparing the phase of a dipole at the origin along Z, simulated in MATLAB (above) vs a dipole simulated in CST (below).

B.4 Single Dipole along X, shifted by 5 cm

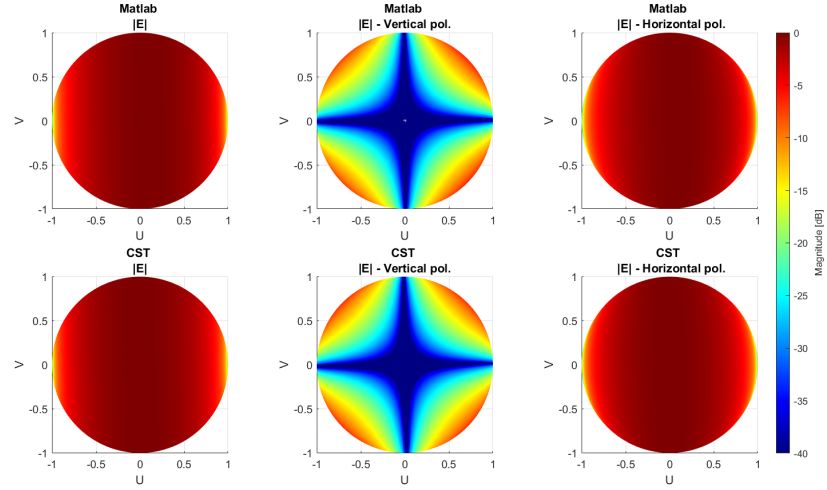


Figure 37: UV plots comparing the magnitude of a dipole shifted by 5 cm from the origin along the x-axis, lying along X, simulated in MATLAB (above) vs a dipole simulated in CST (below).

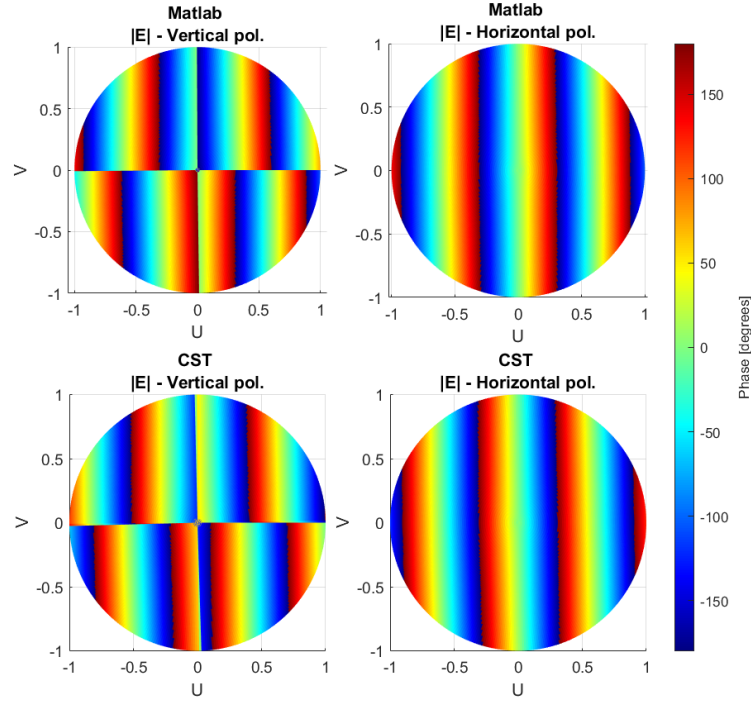


Figure 38: UV plots comparing the phase of a dipole shifted by 5 cm from the origin along the x-axis, lying along X, simulated in MATLAB (above) vs a dipole simulated in CST (below)

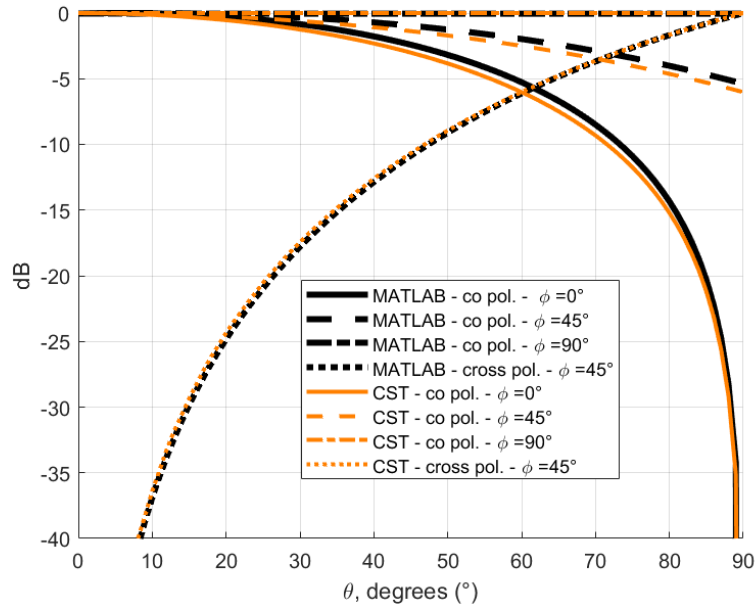


Figure 39: Magnitude cuts comparing the magnitude of a dipole shifted by 5 cm from the origin along the x-axis, lying along X, simulated in MATLAB (black) vs a dipole simulated in CST (orange).

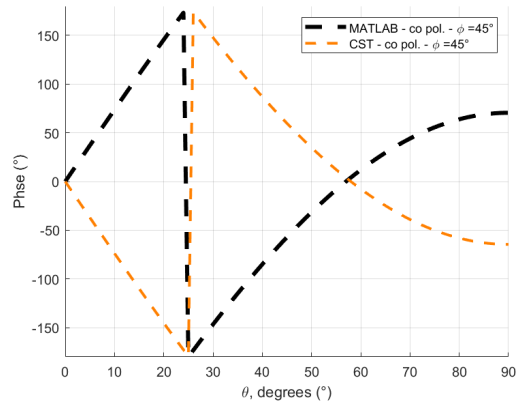


Figure 40: Phase cuts comparing the magnitude of a dipole shifted by 5 cm from the origin along the x-axis, lying along X, simulated in MATLAB (black) vs a dipole simulated in CST (orange).

B.5 Grid of 3x3 dipoles along X spaced by $\lambda/2$, centred at the origin.

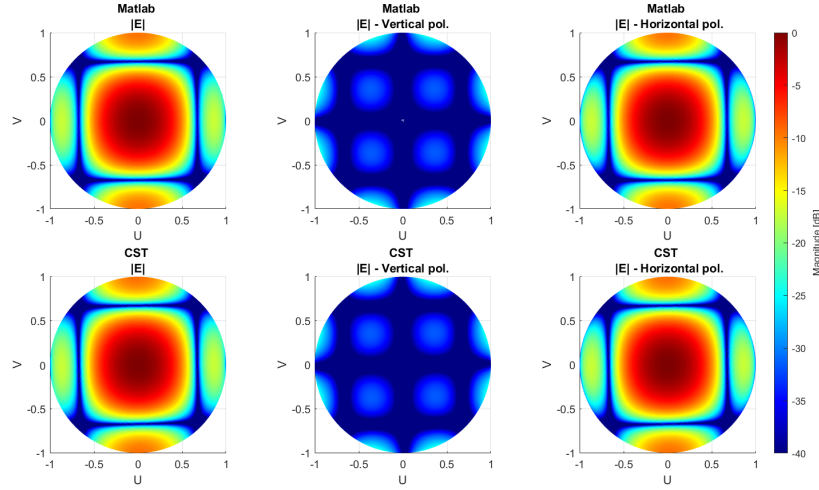


Figure 41: UV plots comparing the magnitude of a 3x3 dipole grid spaced by $\lambda/2$, lying along X, simulated in MATLAB (above) vs a dipole simulated in CST (below)

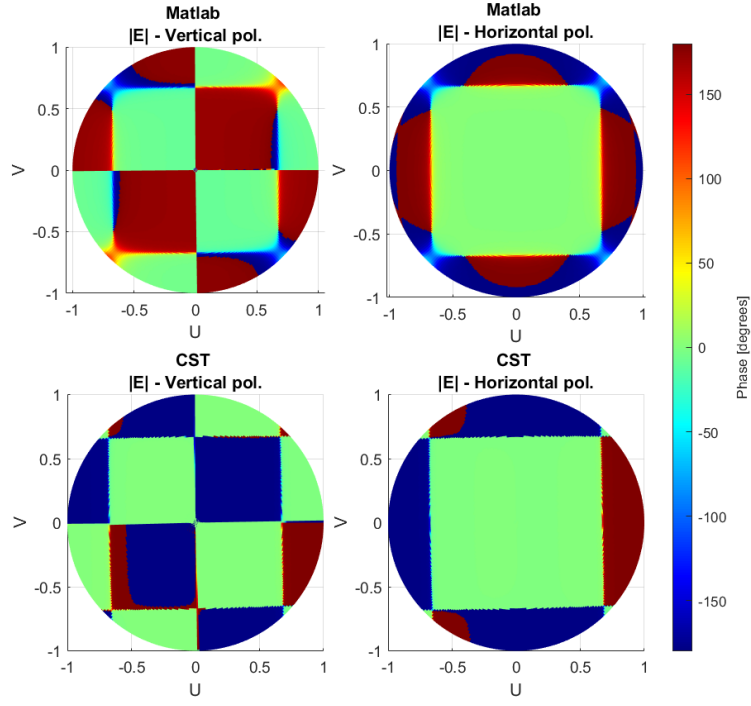


Figure 42: UV plots comparing the phase of a 3x3 dipole grid spaced by $\lambda/2$, lying along X, simulated in MATLAB (above) vs a dipole simulated in CST (below).

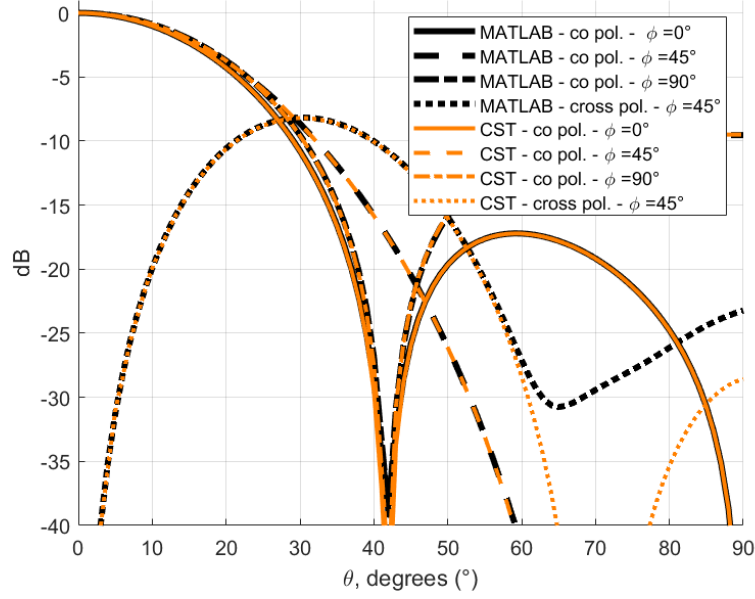


Figure 43: Magnitude cuts comparing the magnitude of a 3x3 dipole grid spaced by $\lambda/2$, lying along X, simulated in MATLAB (black) vs a dipole simulated in CST (orange).

B.6 Horn Antenna at the Origin

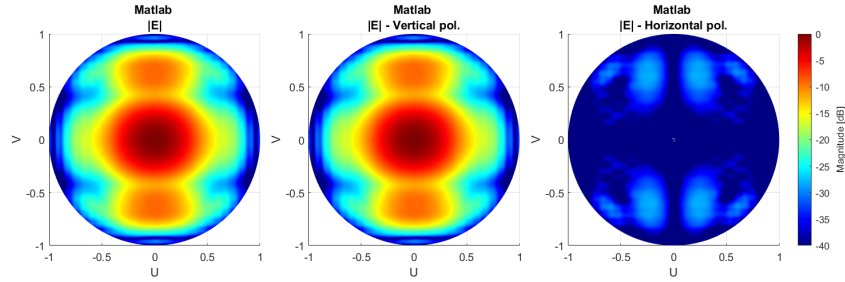


Figure 44: UV plots of the magnitude of a horn antenna at the origin, radiating along +Z. NF samples taken from CST, exported and simulated in MATLAB.

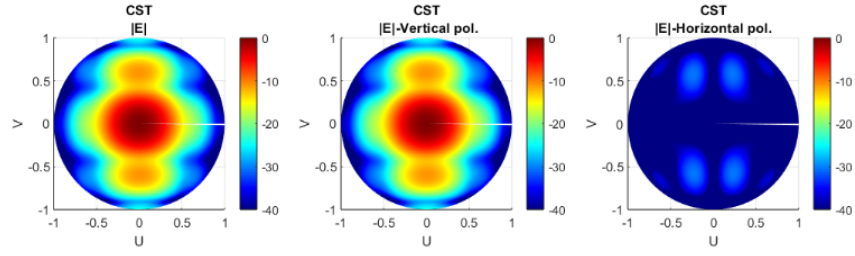


Figure 45: UV plots of the magnitude of a horn antenna at the origin, radiating along $+Z$. Simulated in CST.

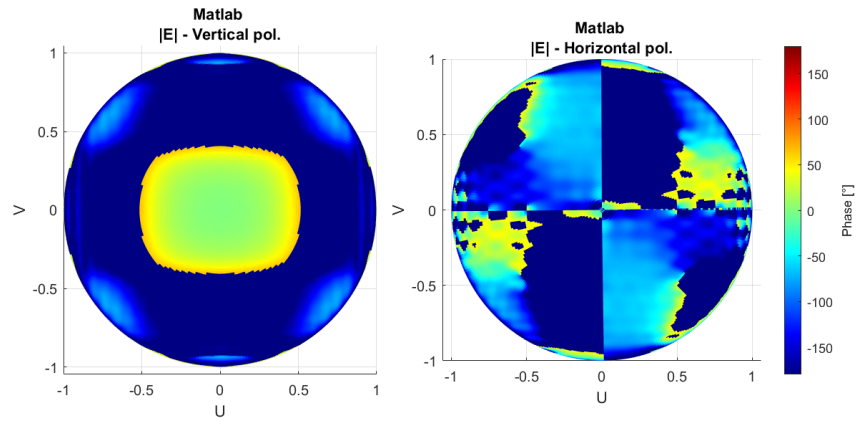


Figure 46: UV plots of the phase of a horn antenna at the origin, radiating along $+Z$. NF samples taken from CST, exported and simulated in MATLAB.

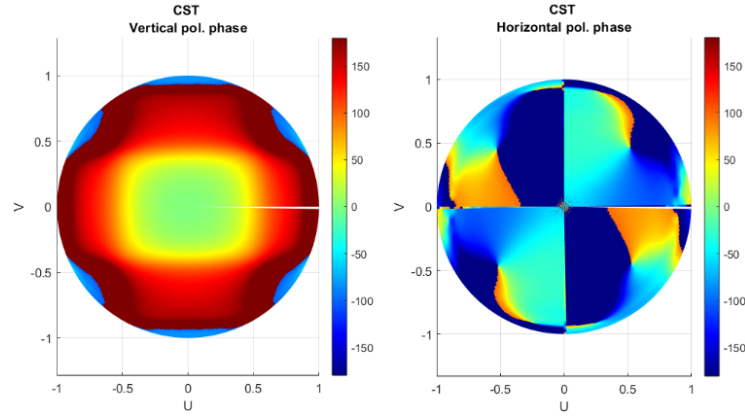


Figure 47: UV plots of the phase of a horn antenna at the origin, radiating along +Z. Simulated in CST.

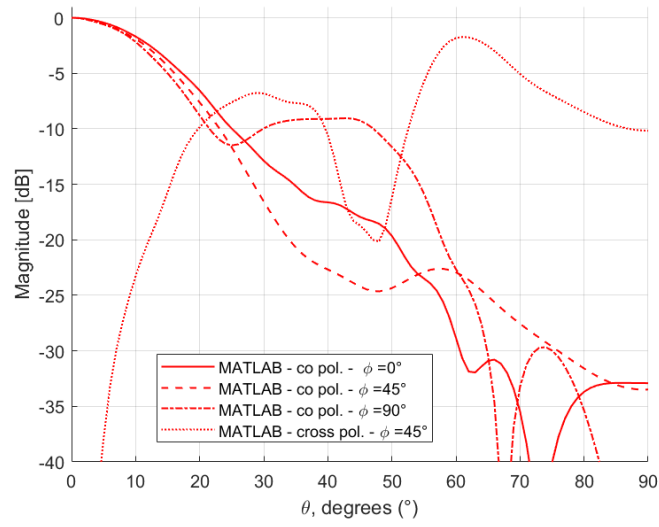


Figure 48: Magnitude cuts of the magnitude of a horn antenna at the origin, radiating along +Z. NF samples taken from CST, exported and simulated in MATLAB.

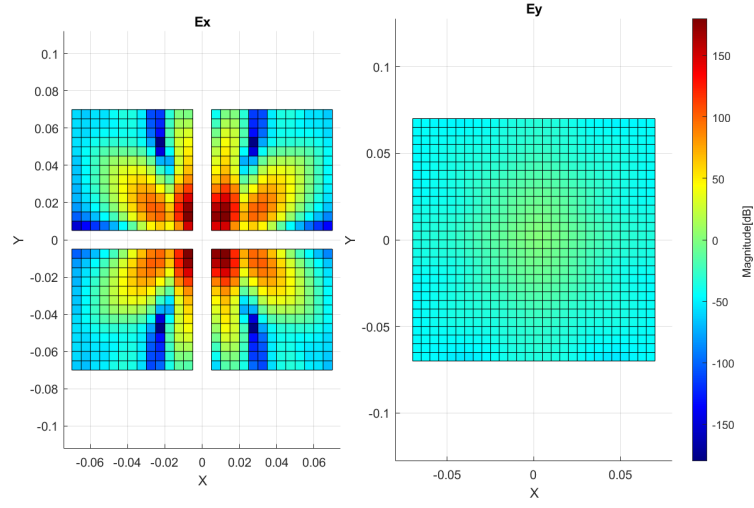


Figure 49: Magnitude of the NF samples taken in CST of the horn antenna at the origin, radiating along +Z.

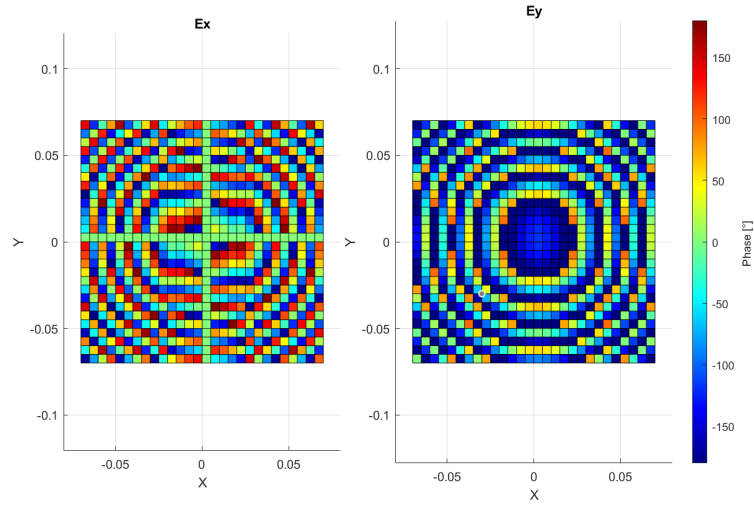


Figure 50: Phase of the NF samples taken in CST of the horn antenna at the origin, radiating along +Z.

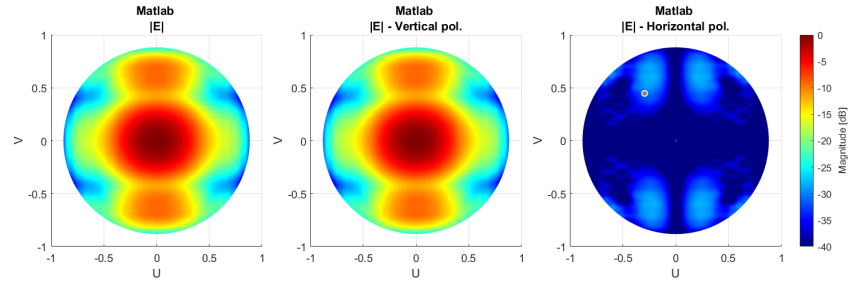


Figure 51: Capped UV plots of the magnitude of a horn antenna at the origin, radiating along +Z. NF samples taken from CST, exported and simulated in MATLAB. Only the valid region is plotted for $\theta = 61.9$.

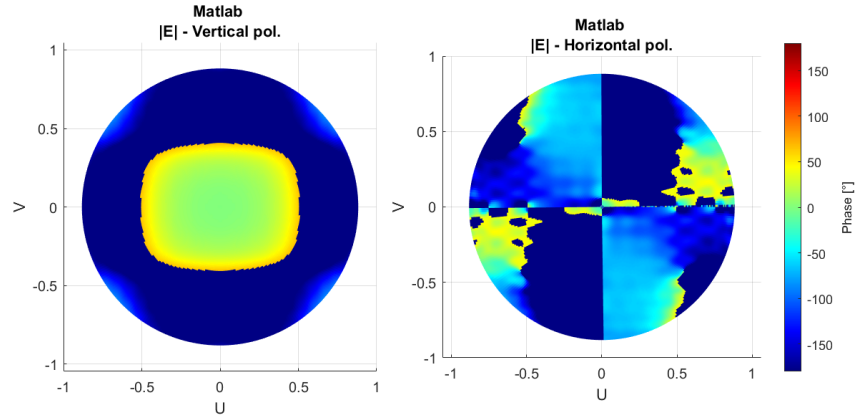


Figure 52: Capped UV plots of the phase of a horn antenna at the origin, radiating along +Z. NF samples taken from CST, exported and simulated in MATLAB. Only the valid region is plotted for $\theta = 61.9$.

B.7 Tilted Horn Antenna at Origin

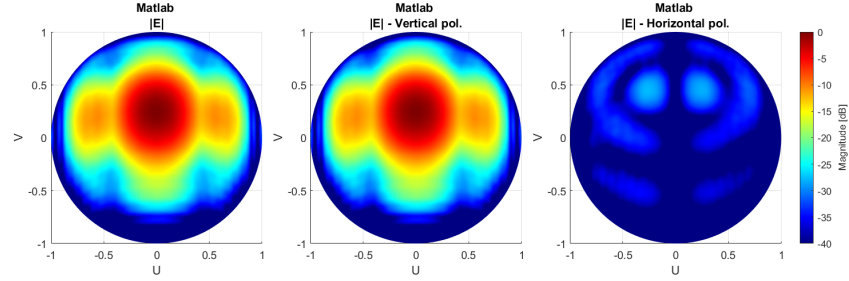


Figure 53: UV plots of the magnitude of a horn antenna at the origin, radiating at 45° from the YZ plane. NF samples taken from CST, exported and simulated in MATLAB.

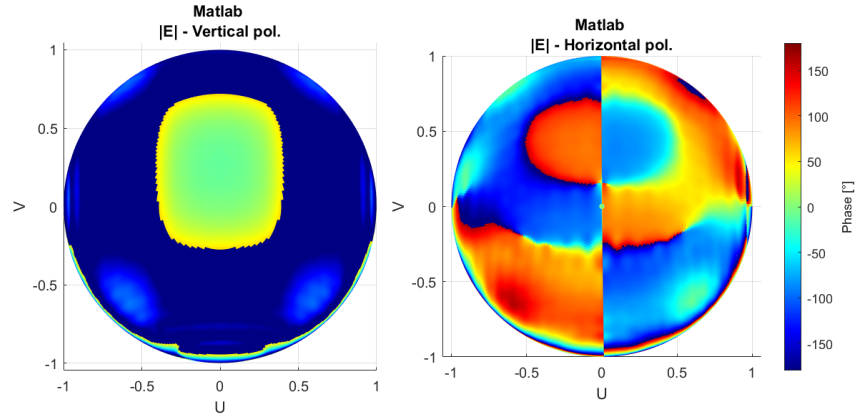


Figure 54: UV plots of the phase of a horn antenna at the origin, radiating at 45° from YZ plane. NF samples taken from CST, exported and simulated in MATLAB.

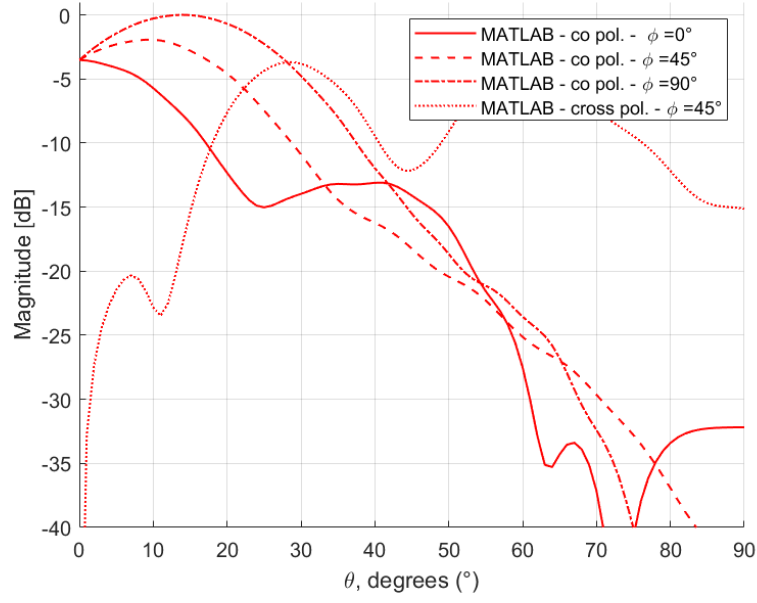


Figure 55: Magnitude cuts of the magnitude of a horn antenna at the origin, radiating at 45° from YZ plane. NF samples taken from CST, exported and simulated in MATLAB.

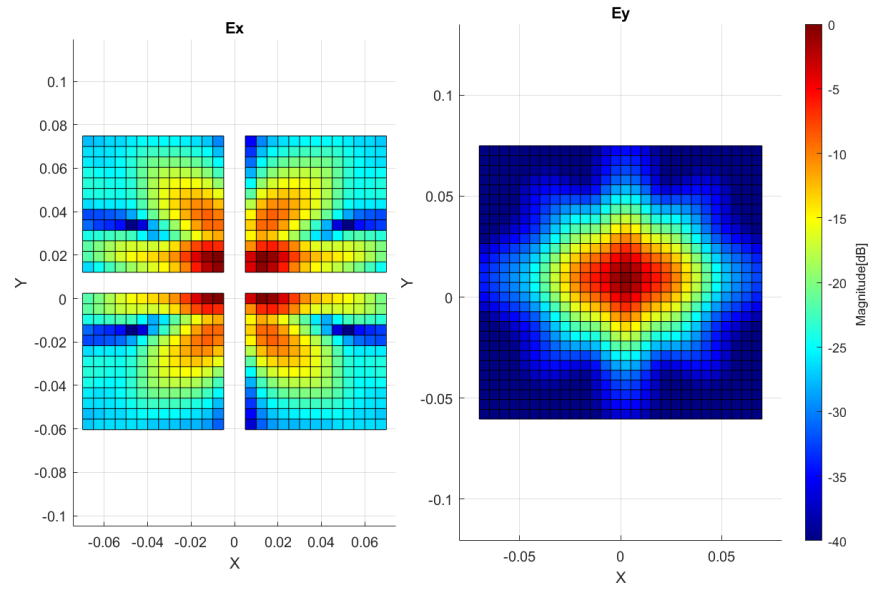


Figure 56: Magnitude of the NF samples taken in CST of the horn antenna at the origin, radiating at 45° from the YZ plane.

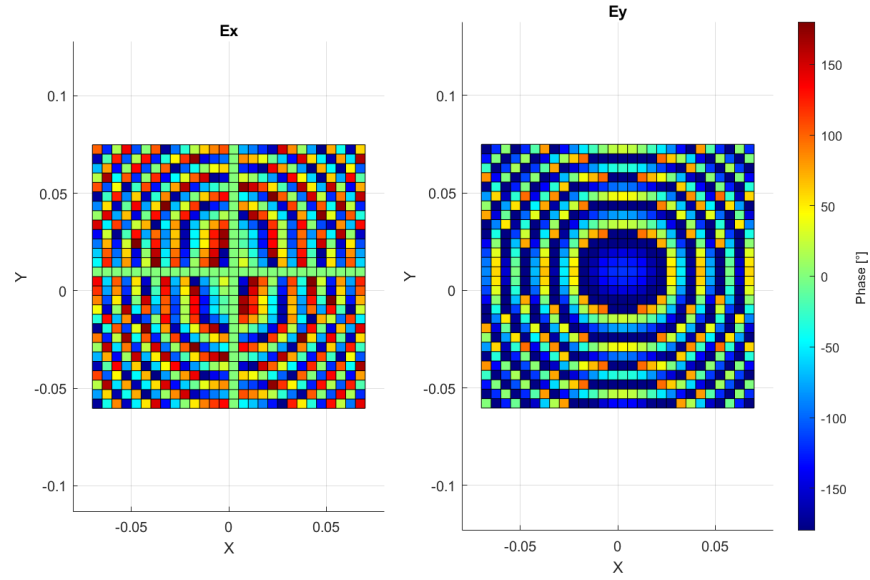
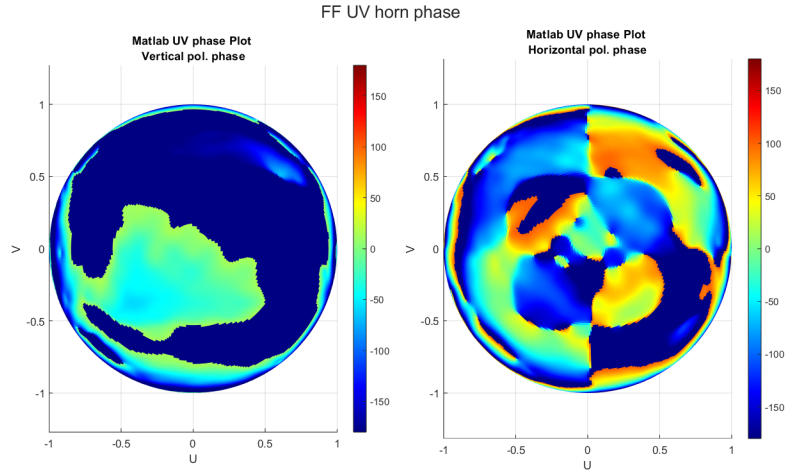


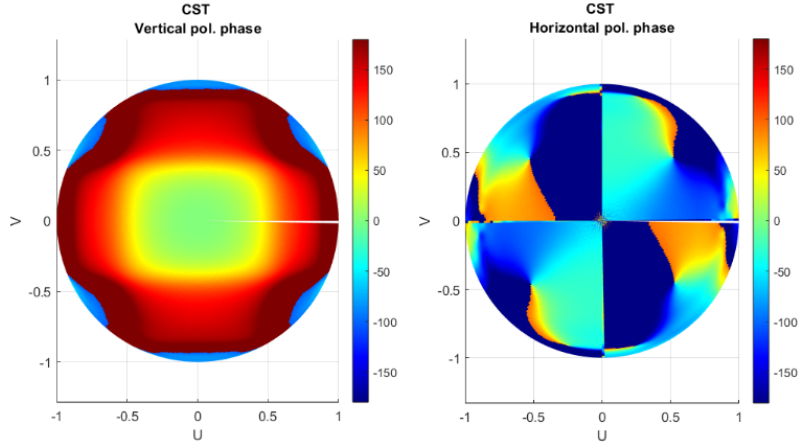
Figure 57: Phase of the NF samples taken in CST of the horn antenna at the origin, radiating at 45° from the YZ plane.

B.8 Experimental Horn Antenna at the Origin

The UV plots of the magnitude can be found in the Results Section at Figure 23.



(a) **Measured** phase of z+ oriented horn [degree].

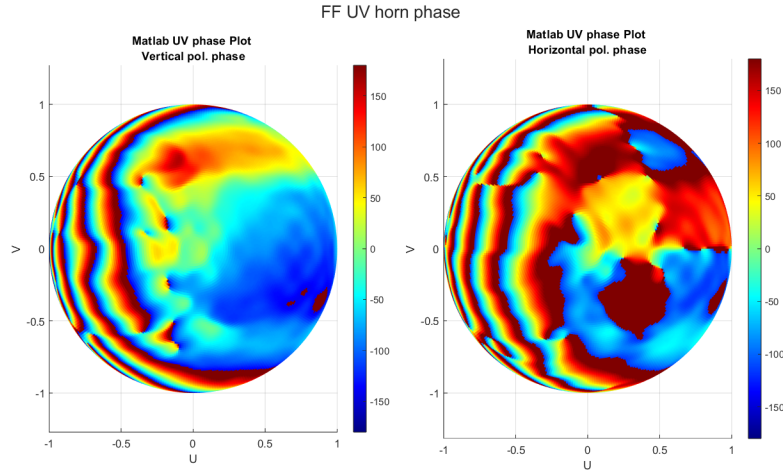


(b) **Simulated** phase of z+ oriented horn [degree].

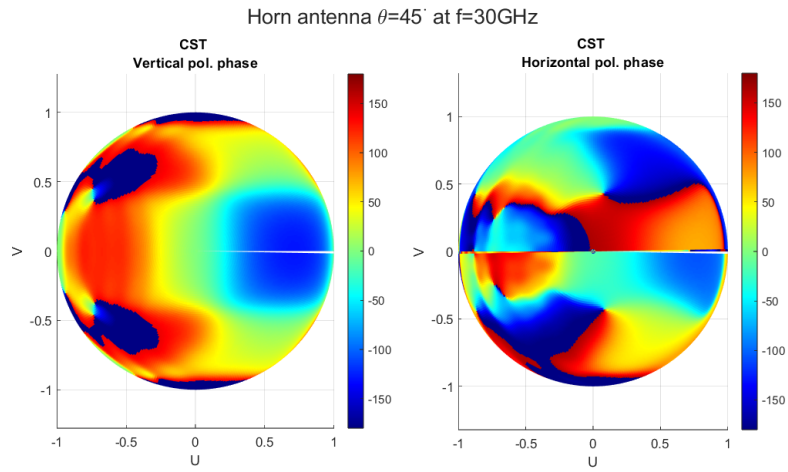
Figure 58: MATLAB and CST comparison of phase of z+ oriented horn.

UV plots of the phase of a horn antenna at the origin, radiating along +Z. Experimental NF samples exported and simulated in MATLAB.

B.9 Experimental Tilted Horn Antenna at the Origin

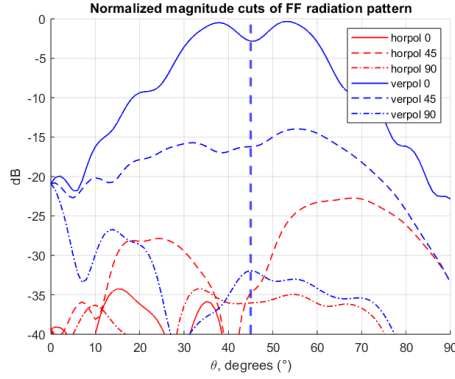


(a) Experimental far-field phase of 45 degree oriented horn [degree].

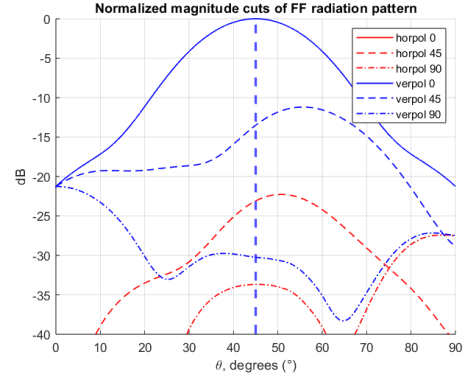


(b) CST Simulated far-field phase of 45 degree oriented horn [degree].

Figure 59: UV phase comparison of the phase of tilted horn antenna at 45° from the XZ plane oriented horn. Experimental data exported and simulated in MATLAB.



(a) Measured horn far-field cuts (NFtoFF-transformed).



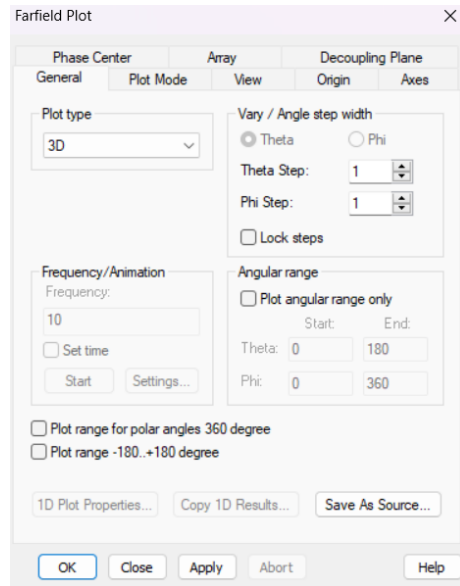
(b) Simulated horn far-field cuts (CST).

Figure 60: Comparison of the Magnitude cuts of a horn antenna at the origin, radiating at 45° from the XZ plane for simulated and experimental radiation. Experimental NF samples exported and simulated in MATLAB.

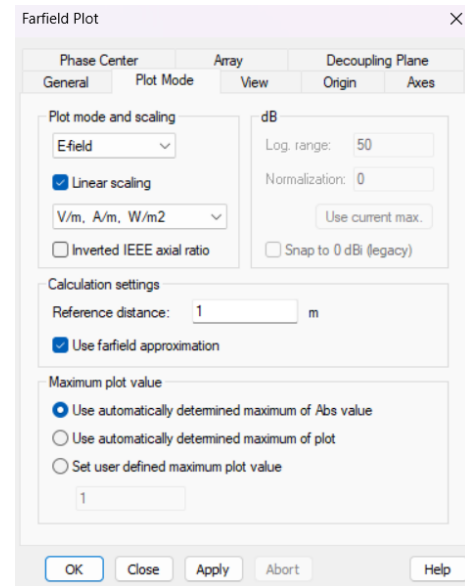
C CST simulations

C.1 CST export setting

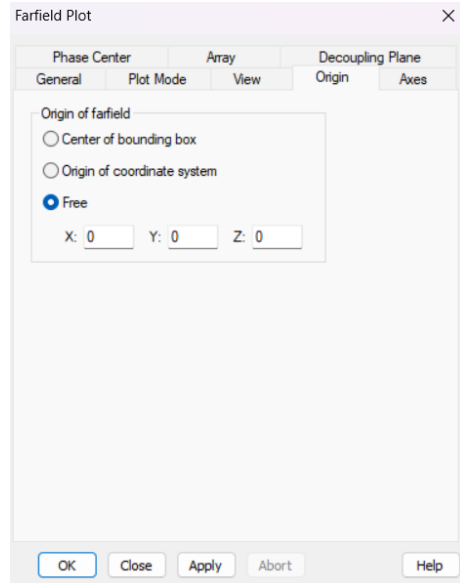
Before exporting CST results to process in MATLAB, the following far-field plot properties were chosen.



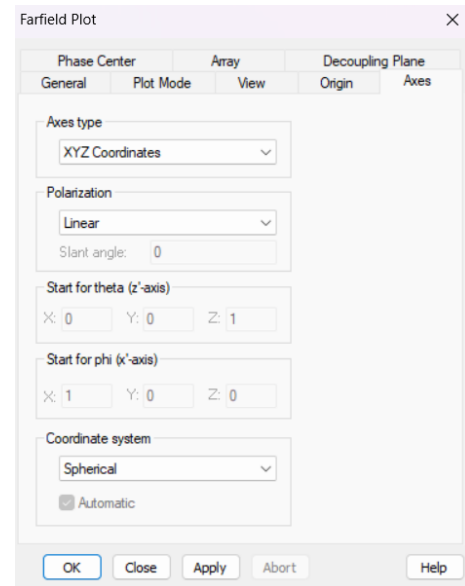
(a) Far-Field plot properties: general.



(b) Far-Field plot properties: plot mode.



(c) Far-Field plot properties: origin settings.



(d) Far-Field plot properties: axis.

Figure 61: Overview of CST Far-Field Plot Configuration.

The following settings describe the *Result Templates* export settings

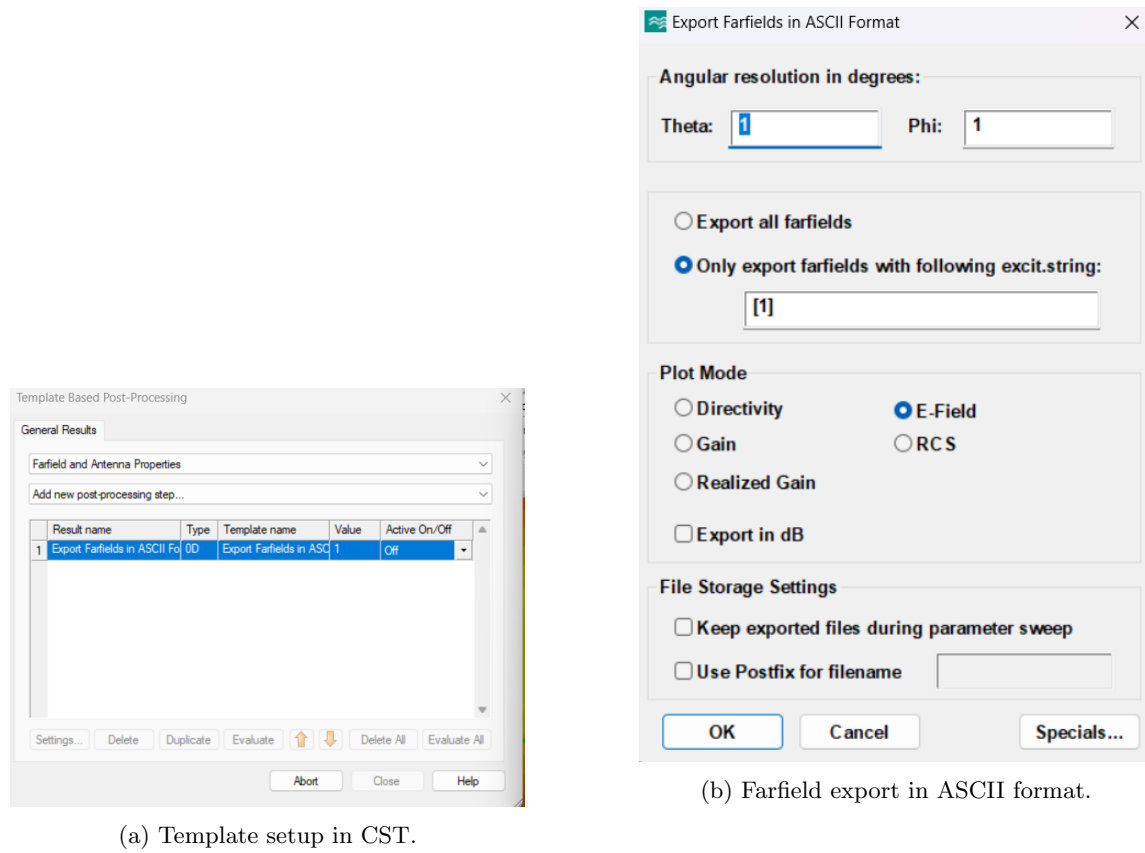


Figure 62: CST setup for template and far-field data export.

C.2 CST data, plot by MATLAB

The output of exported data from MATLAB

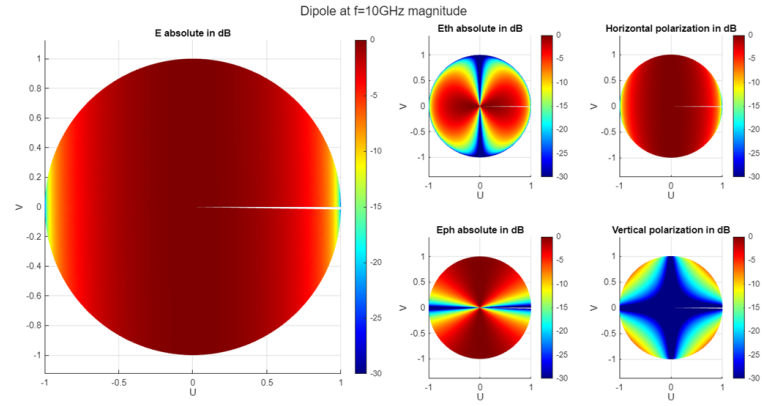


Figure 63: UV magnitude short dipole oriented along x at the origin.

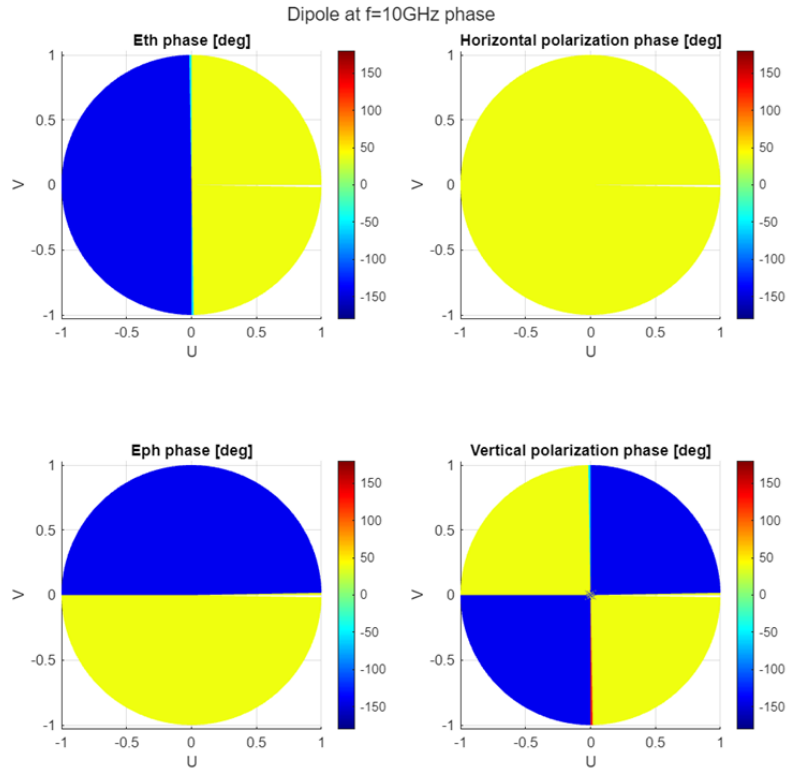


Figure 64: UV phase short dipole oriented along x at the origin.

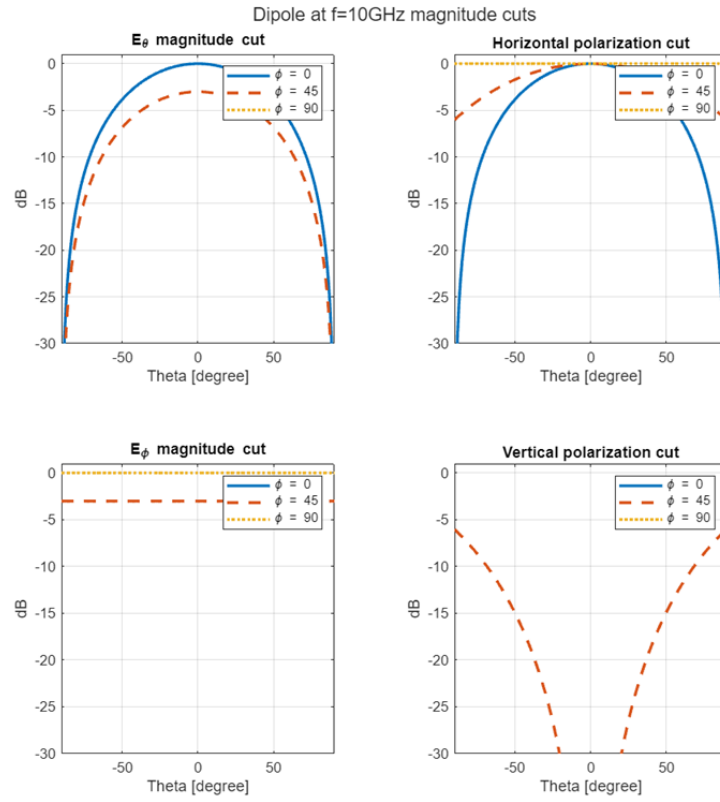


Figure 65: Constant ϕ cut magnitude short dipole oriented along x at the origin.

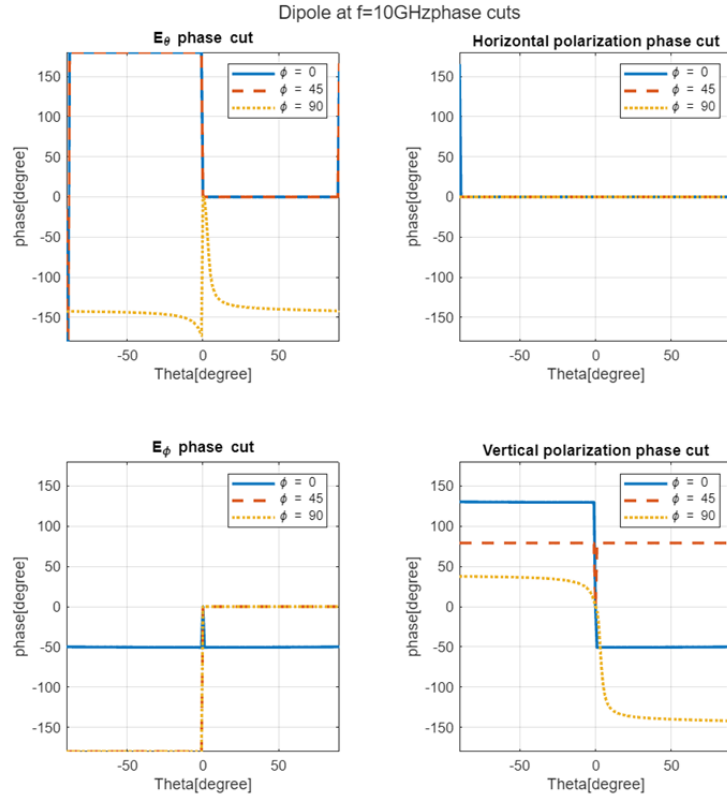


Figure 66: Constant ϕ cut phase short dipole oriented along x at the origin.

C.3 Near-field export settings

Export 3D Field Result

Field Result

E-FieldVe-field (f=30) [1] Browse Results...

Set Frq / Time... Browse All...

Export Settings

☐ 3D Export in Volume

☐ 3D Export on Surfaces

☐ Export Field on Pointlist

☒ Export Field on 2D Plane

Normal: ☐ X ☐ Y ☒ Z

Position: 28

Stepsize: 300/30/2

☐ Use Subvolume

Xmin:	Xmax:
-20.55	20.55
Ymin:	Ymax:
-16.425	16.425
Zmin:	Zmax:
-73.605	30.0816456506

File location of pointlist

☐ relative to Master-Projectpath BrowseFile...

File Options

☒ ASCII ☐ Use Prefix

☐ HDF5 (.h5) ☐ Use Postfix

OK Cancel Specials... Help

Figure 67: 3D field export settings.

C.4 Rotated Far-Field

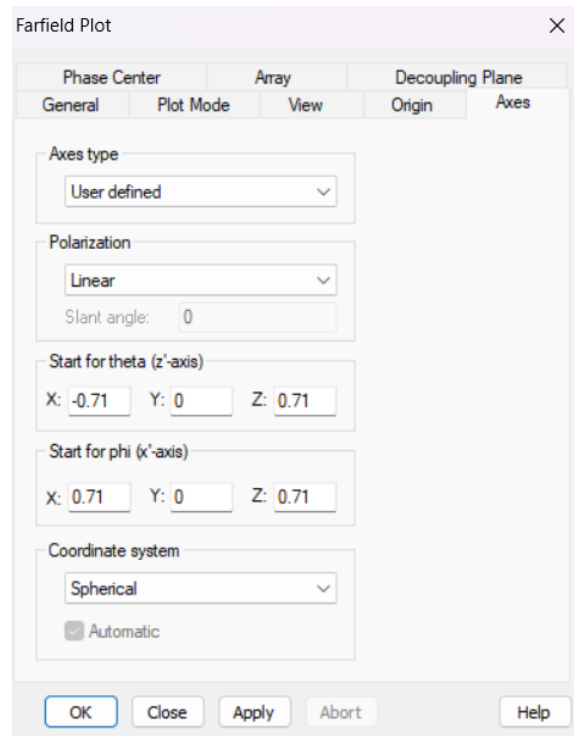


Figure 68: Far-Field with rotated reference system.

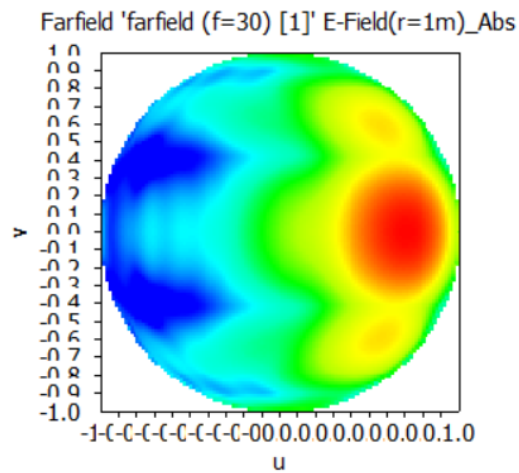


Figure 69: UV plot of rotated far-field of horn antenna from CST.